Mechanism and Machine Theory 219 (2026) 106317

Contents lists available at ScienceDirect

Mechanism and Machine Theory

journal homepage: www.elsevier.com/locate/mechmt

Research paper

A revised framework for ball-screw contact kinematics

Pello Alberdi, Aitor Arana, Aitor Oyanguren, Jon Larrañaga, Ibai Ulacia *

Faculty of Engineering, Mechanical and Industrial Production Department, Mondragon Unibertsitatea, Arrasate-Mondragon, Spain

ARTICLE INFO

Keywords:
Ball screws
Contact kinematics
Rolling slip
Side slip
Spinning slip

ABSTRACT

Ball screw mechanisms are widely used in precision applications due to their high stiffness and efficiency. However, unlike ball bearings, the helical geometry of ball screws leads to multidirectional contact kinematics, which significantly influence friction, wear, and overall performance. In the classical contact kinematic formulation, the velocity components of the ball are not fully projected onto the contact interface, resulting in significant errors in the calculation of contact kinematics.

This work presents a revised contact kinematic formulation considering all the missing components, and revealing substantial differences in the prediction which alters the conventional understanding of contact kinematics in ball screws. The contact kinematics are broken down into their fundamental components-rolling, side, and spinning slip-and analytical expressions for each are introduced. A new characterisation framework based on three independent variables is proposed, quantifying the distinct effects of rolling, side, and spinning motion more comprehensively than traditional single *SRR*.

The proposed model is first validated against a well-established ball bearing formulation (i.e. ball screw with no lead), confirming its accuracy under such geometry. At the ball screw scale, the results reveal substantial deviations from existing models. Side slip emerges as the dominant mechanism, fundamentally revising the conventional interpretation of contact kinematics. Furthermore, the new three-variable framework enables a more complete and accurate characterisation of the contact behaviour, offering valuable insights for tribological modelling and performance optimisation. Finally, a parametric analysis is conducted to examine the influence of key kinematic constraints on the sliding behaviour, highlighting the independent role of each in defining the contact kinematics.

1. Introduction

Ball screw mechanisms are mechanical components that convert rotational motion into linear displacement or vice versa. They are widely used in industrial applications such as machine tools and automation systems due to their high positioning accuracy and efficiency [1–4]. Unlike power screw mechanisms, ball screws incorporate balls that roll between raceways, significantly reducing friction and improving mechanical efficiency [5,6].

Ball screws operate in demanding environments such as precision machine tools, aerospace actuators, and advanced automation systems, where accurate prediction of dynamic performance, durability, and service life is essential. Meeting these requirements is

* Corresponding author.
E-mail address: iulacia@mondragon.edu (I. Ulacia).

https://doi.org/10.1016/j.mechmachtheory.2025.106317
Received 11 October 2025; Received in revised form 15 November 2025; Accepted 5 December 2025
Available online 16 December 2025

Nomenclature

(O, X, Y, Z)	Absolute coordinate system
(o', x', y', z')	Relative coordinate system of the ball
(o, t, n, b)	Frenet-Serret coordiante system
$(o_{i/o}, x_{i/o}, y_{i/o}, z_{i/o})$	Coordinate system of the contact
$\mathbf{A}^{01}$	Transform matrix from the absolute coordinate system to the relative coordinate system
$\mathbf{A}^{12}$	Transform matrix from the relative coordinate system to the Frenet coordinate system
$\mathbf{A}^{23i}$	Transform matrix from the ball coordinate system to the inner contact coordinate system
$\mathbf{A}^{23o}$	Transform matrix from the ball coordinate system to the outer contact coordinate system
a_H	Semi-major axis of the contact ellipse [mm]
b_H	Semi-minor axis of the contact ellipse [mm]
D	Diameter of the ball [mm]
d_m	Pitch diameter [mm]
$\hat{E}$	Complete elliptic integral of the second kind
F_a	External axial load [N]
k	Ellipticity parameter
L	Pitch [mm]
$R_{i/o}$	Radius of curvature of the inner/ outer deformed surface [mm]
$\hat{R_{i/o}}$	Equivalent radius of curvature [mm]
r_m	Pitch radius [mm]
$r_{i/o}$	Inner/ outer raceway curvature radius [mm]
$r'_{i/o}$	Pure rolling radii [mm]
$\mathbf{r}^0_{oo'}$	Position vector from the origin to the centre of the ball
r_{nut}	Principal curvature radii of the nut
r_{screw}	Principal curvature radii of the screw
$S_{i/o}$	Distance from the centre of the ball to a point of the deformed surface [mm]
SRR	Slide-to-Roll Ratio [%]
S_p	Spin-to-roll ratio [-]
v_e	Entrainment speed [m/s]
v_{ball}	Velocity of the ball within the contact surface [m/s]
v_{nut}	Velocity of the nut within the contact surface [m/s]
v_{roll}	Rolling slip distribution [m/s]
v_s	Sliding velocity within the contact surface [m/s]
v_{screw}	Velocity of the screw within the contact surface [m/s]
v_{side}	Side slip distribution [m/s]
v_{sp}	Spinning slip distribution [m/s]
ω	Rotational speed of the screw [rad/s]
ω_m	Orbital speed of the ball [rad/s]
ω_R	Angular speed of the ball about its own axis [rad/s]
ω_{sp}	Spinning speed of the contact [rad/s]
ω_t, ω_n, ω_b	Components of spinning angular velocity in t-, n-, b-directions, respectivelly
$\alpha_{i/o}$	Inner/ outer contact angle [°]
α^0	Nominal contact angle [°]
β	Pitch angle [°]
β'	Yaw angle [°]
θ	Angular rotation of the Frenet-Serret coordinate [°]
ψ	Helix angle [°]
ϕ	SRR angle [°]
γ	Entrainment speed angle [°]

challenging because their behaviour is strongly influenced by complex tribological phenomena, efficiency losses, and progressive wear. High-fidelity theoretical models are therefore indispensable, not only for providing physical insight and guiding design optimisation but also for enabling performance assessment, lifetime estimation, and condition-based maintenance strategies [7]. More recently, these models have become key enablers of data-driven approaches for condition monitoring, prognosis, and health management [8,9]. Advances in artificial intelligence have further expanded this role, with emerging techniques, [10–12], highlighting the importance of reliable physical models as foundations for predictive maintenance. Within this context, accurate modelling of ball-screw contact kinematics is critical, as they directly govern wear [13] and power losses [14].

The helical structure of ball screws introduces complexities in kinematic analysis of the balls. The multidirectional motion of the ball leads to a non-uniform sliding speed distribution, which includes simultaneous slips in the rolling and transverse direction, as well as the spinning motion within the contact interface. Early studies on ball screw kinematics were based on simplifying assumptions regarding the motion of the balls. Levit [15] and Drozdov [16] analysed the system under the assumption of a no-slip condition, implying that the balls roll without sliding across the contact surface.

The first comprehensive theoretical work of contact kinematics was presented by Lin et al. [17], who derived mathematical expressions to calculate the sliding speed distribution across the deformed elliptical contact. Their study demonstrated that both rolling and sliding occur simultaneously at the contact interface, refuting the previously assumed no-slip condition. Lin's formulation essentially described the contact interface kinematics on the basis of an assumed load state and global motion of the ball. However, these state of the ball were not defined within their framework.

This was later completed by Wei and Lin [18], who developed a comprehensive quasi-static model that simultaneously described the load state and global motion of the ball. They calculated the load of the ball from elastic deformation and contact angle variations, considering inertial forces. The absolute velocity of the ball were described by introducing equations to calculate the orbital speed (ω_m) and the rotational speed of the ball (ω_R). This study made a key contribution to the contact kinematic modelling of ball screws. Building on Lin's formulation [17], they proposed the Slide-To-Roll Ratio (*SRR*) as a parameter to quantify sliding in ball screw contacts. The *SRR* is a fundamental parameter in tribology and contact mechanics, commonly used to link contact conditions to key tribological properties such as friction, wear, and lubrication performance [19–21]. Since its introduction by Wei and Lin [18], the *SRR* has been widely adopted in ball screws as a key indicator of sliding behaviour [18,22–30]. However, the *SRR* values obtained in their study were unusually high for rolling elements [31,32], raising questions about the accuracy of their expressions [29].

Following these two foundational works, both contact load and motion of the ball have been extensively investigated in the literature, through quasi-static and dynamic solving strategy schemes [33–36]. The contact load have been extensively analysed at different modelling strategies. For example, at high axial loads, the elastic deformations of the nut and screw and generate a non-uniform load distribution of the ball through the screw. In order to study load states, finite element-based approaches (FEM) have been implemented in the literature [37–42]. By contrast, the kinematics phenomena has consistently been analysed building on the theoretical frameworks of Lin et al. [17] and Wei and Lin [18]. Since contact kinematics play a critical role in predicting a wide range of physical phenomena, these works have therefore served as the foundation for numerous studies. These include investigations into friction torque and efficiency under various conditions [43–48], drag torque behaviour [3,49], lubricated contact performance [22,27,30,50], thermo-mechanical modelling [26], and wear prediction [25,28,51–54].

Although the formulations of Lin et al. [17] and Wei and Lin [18] have been widely adopted in the ball screw literature, recent studies have identified certain inaccuracies. Wang et al. [29] found limitations in the contact kinematic formulation, stating that the linear velocity component of the ball through the raceways is not accurately calculated. They then compared this approach against the work of Harris [31] on ball bearings, finding good agreement with the latter and demonstrating that Lin's method significantly overestimates the sliding speed of the contact. Recently, the authors of the present work [55] demonstrated that the equations proposed by Wei and Lin [18] for calculating the orbital speed (ω_m) and rotational speed (ω_R) of the ball do not account for the transverse slip component of the raceway. To address this limitation, new equations were derived and experimentally validated, showing that the errors in the classical formulation become particularly significant at high helix angles.

However, while our previous research redefined and validated the description of the absolute motion of the ball, the classical formulation of Lin et al. [17], which transforms this global motion into the contact interface kinematics, remains incomplete. Specifically, the velocity components of the ball are not fully projected onto the contact surface, leading to an incomplete description of the contact-level kinematics. By incorporating the missing terms, the revised formulation presented in this work yields a sliding distribution that departs fundamentally from the classical model.

In contrast to the prevailing understanding, the accurate computation of contact kinematics reveals that side and spinning slip components play a far more substantial role in sliding speed distribution. This multidirectional sliding behaviour at the contact interface is not unique to ball screws but has also been identified in mechanical systems such as hypoid gears, Wildhaber-Novikov gears, and continuously variable transmissions (CVTs) [56–60]. It has also gained increasing relevance in the field of contact tribology [61–64]. In these fields, the limitations of the single *SRR* as a quantifying parameter have long been recognised, leading to the introduction of additional indicators to characterise rolling, side, and spinning slip effects [65–69]. Despite these advances, however, ball screw analyses in the literature continue to rely exclusively on the single *SRR* to quantify contact kinematics. This underscores the need for a revised quantification framework able to capture the full complexity of contact kinematic behaviour in ball screw mechanisms.

This paper revises the contact kinematic formulation of Lin et al. [17], which has served as the fundamental reference in the literature for several decades, thereby changing the previous understanding of contact kinematics and introducing a substantial theoretical advancement in the field. The revised formulation addresses the identified inaccuracies in the mathematical foundations of the classical approach, and offers a comprehensive framework for calculating the sliding speed distribution over the contact surface. Furthermore, the sliding speed is broken down into its fundamental components-rolling, side, and spinning slip-and analytical expressions for each are introduced. Finally, a new framework is proposed to quantify the sliding speed at the contact. Rather than relying on a single *SRR* parameter, three independent variables are introduced that capture the contact kinematics, providing a complete and unambiguous description of sliding behaviour.

Based on this revised theoretical formulation, the present work addresses the following specific objectives:

- Compare the contact kinematics predicted by the classical literature formulation and the revised model proposed in this work, across two configurations: angular contact ball bearing and ball screw geometries.
- Compare the limitations and advantages between single *SRR* and the proposed three-parameter approach.
- Analyse the individual influence of kinematic constraints-pure rolling radius, pitch angle, and yaw angle-on the contact kinematics.
- Discuss the influence of different methodologies for predicting these kinematic constrains under varying operating conditions.

2. Theoretical model development

In this section, the theoretical basis of the revised contact kinematic formulation is presented. The formulation is constructed under the following general assumptions:

- The motion is analysed under steady-state conditions, at constant orbital and rotational speeds.
- The ball and raceways are treated as elastic bodies, and plastic deformations are not included in the formulation.
- The component-level geometrical dimensions are much larger than the contact interface features. Consequently, Hertzian contact theory and Ertel-Grubin assumptions can be applied: (i) the contact surfaces are assumed to be paraboloid, smooth and continuous, and (ii) film thickness is considered constant with minor dimensional variations that arise from lubricant film thickness being neglected.

2.1. Definition of the coordinate systems

The kinematic model of the ball screw mechanism is constructed using four coordinate systems, as illustrated in Fig. 1:

(1) Absolute coordinate system $[O, X, Y, Z]$: The origin O is fixed in space and located at one end of the screw. The Z axis is collinear with the rotation axis of the screw.
(2) Relative coordinate system of the ball $[o', x', y', z']$: The origin o' coincides with the absolute coordinate system's origin. The z' axis is parallel to the screw axis, while the x' axis is obtained by rotating the X axis of the absolute system by an angle θ about the z' axis. The x' axis lies in the $x'y'$ plane and coincides with the projection of the ball's centre. The angle θ determines the angular position of the ball centre within the $x'y'$ plane.
(3) Frenet-Serret coordinate system $[o, t, n, b]$: The origin o is placed at the ball's centre. The n axis is aligned with the x' axis of the ball's coordinate system. The t axis is tangential to the ball trajectory and inclined by the helix angle ψ with respect to the y' axis.
(4) Contact coordinate system $[o_{i/o}, x_{i/o}, y_{i/o}, z_{i/o}]$: The origin o is located at the centre of the contact ellipse. The x axis aligns with the semi-minor axis of the ellipse, and the z axis is normal to the contact surface, pointing towards the ball centre. As the inner and outer contact points lie in the nb plane of the Frenet-Serret system, two such systems are defined per ball-distinguished by the subscripts i (inner) and o (outer).

2.2. Transformation matrices

To develop the theoretical kinematic formulation, the transformation relationships between the defined coordinate systems has to be established [23].

The transformation matrix from the absolute coordinate system and the relative coordinate system of the ball is given by:

$$\mathbf{A}^{01} = \begin{bmatrix} \cos\theta & \sin\theta & 0 \\ -\sin\theta & \cos\theta & 0 \\ 0 & 0 & 1 \end{bmatrix} \tag{1}$$

where θ is the angular displacement between the two coordinate systems.

The transformation from the relative ball coordinate system to the Frenet-Serret system is expressed as:

$$\mathbf{A}^{12} = \begin{bmatrix} 0 & \cos\psi & \sin\psi \\ -1 & 0 & 0 \\ 0 & -\sin\psi & \cos\psi \end{bmatrix} \tag{2}$$

where ψ is the helix angle.

The transformation from the Frenet-Serret system to the contact coordinate system (inner or outer) is defined as:

$$\mathbf{A}^{23k} = \begin{bmatrix} \pm 1 & 0 & 0 \\ 0 & \sin\alpha_k & \cos\alpha_k \\ 0 & \mp\cos\alpha_k & \pm\sin\alpha_k \end{bmatrix} \quad (k = i, o) \tag{3}$$

where α_k denotes the contact angle. The subscript i refers to the inner contact and o to the outer contact. The upper sign of $\pm$ or $\mp$ operand corresponds to the inner contact case while the lower sign refers to the outer contact. This criteria is maintained throughout the whole paper. All transformation matrices presented above convert vectors in the forward direction. The inverse transformations are obtained using the matrix transpose, as all matrices are orthogonal ($[\mathbf{A}]^{-1} = [\mathbf{A}]^{\mathrm{T}}$).

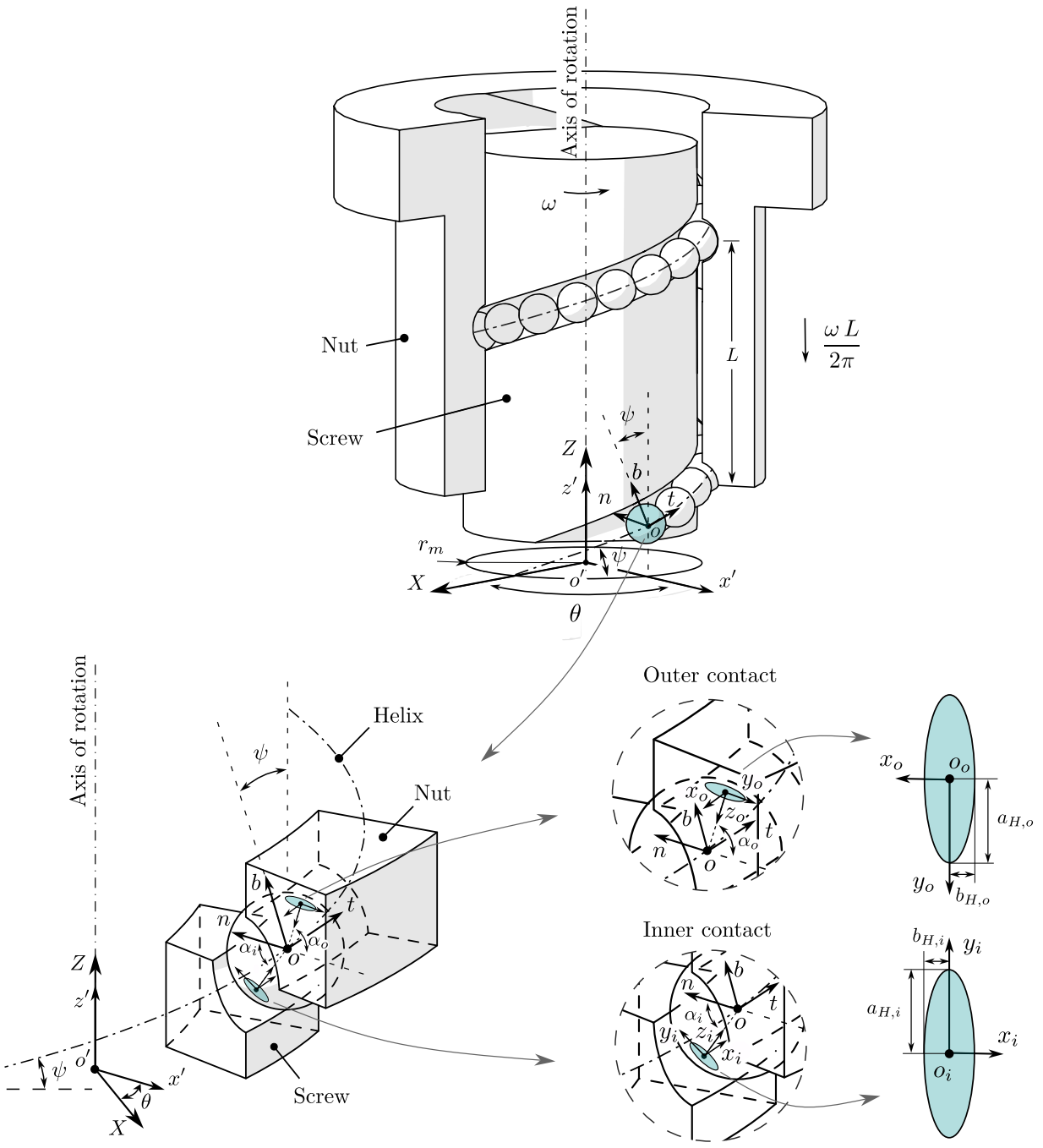

Fig. 1. Absolute, relative, front-serret and contact coordinate systems of the ball screw mechanism.

2.3. Definition of the contact surface

When two non-conformal solids are loaded against each other, the bodies deform elastically, generating a finite contact area. In ball screws, this area is elliptical (see Fig. 1). The relative motion of the contacting bodies within this region gives rise to the sliding speed distribution, which defines the contact kinematics. According to Hertz's elastic contact theory, the semi-major and semi-minor axes of the inner and outer contact ellipses are given by [70]:

$$a_{H,k} = \left(\frac{6k^2 \hat{E} W_k \hat{R}_k}{\pi E'} \right)^{1/3} \quad (k = i, o) \tag{4}$$

$$b_{H,k} = \left(\frac{6\hat{E} W_k \hat{R}_k}{\pi E' k} \right)^{1/3} \quad (k = i, o) \tag{5}$$

where W_k is the normal load at the inner or outer contact, k is the ellipticity parameter, E' is the equivalent elastic modulus, $\hat{E}$ is the complete elliptic integral of the second kind, and $\hat{R}_k$ is the equivalent radius of curvature of the contacting bodies.

The parameter $\hat{R}_k$ plays a central role in the methodological improvement, as it is directly affected by the groove curvature definition. It is obtained from the principal curvature radii in the x and y directions as:

$$\frac{1}{\hat{R}_k} = \frac{1}{\hat{R}_x} + \frac{1}{\hat{R}_y}. \quad (k = i, o). \tag{6}$$

For the nut-ball contact:

$$\frac{1}{\hat{R}_o} = \left(\frac{1}{r_{ball,x}} + \frac{1}{r_{nut,x}} \right) + \left(\frac{1}{r_{ball,y}} + \frac{1}{r_{nut,y}} \right) \tag{7}$$

and for the screw-ball contact:

$$\frac{1}{\hat{R}_i} = \left(\frac{1}{r_{ball,x}} + \frac{1}{r_{screw,x}} \right) + \left(\frac{1}{r_{ball,y}} + \frac{1}{r_{screw,y}} \right) \tag{8}$$

In these equations, the ball curvature radii are $r_{ball,x} = r_{ball,y} = D/2$, where D is the diameter of the ball. The groove curvature radii are typically approximated as $r_{screw,y} = -r_i$ and $r_{nut,y} = r_o$, with r_i and r_o being the inner and outer raceway groove radii, respectively. In the literature, the groove curvature in the x-direction is commonly approximated using ball-bearing geometry assumptions, which neglect the specific influence of the groove profile and the helix angle.

To overcome this limitation, Bertolino et al. [71,72] derived exact analytical expressions for calculating the principal curvature radii of the grooves. In their work, the equations were obtained using a differential-geometry approach that accounts for the helix angle and a gothic-arch groove profile. Simplified approximate formulations were also proposed to reproduce the exact solution under the assumption of a circular groove profile, yielding curvature radii with negligible error. In this approach, the curvatures in the x-direction are expressed as:

$$r_{nut,x} = -\frac{r_m + r_o \cos\alpha_o \cos^2\psi}{\cos\alpha_o \cos^2\psi}, \tag{9}$$

$$r_{screw,x} = \frac{r_m - r_i \cos\alpha_i \cos^2\psi}{\cos\alpha_i \cos^2\psi} \tag{10}$$

where r_m is the pitch radius, and ψ is the helix angle. By adopting this improved curvature model, the present analysis enhances the geometric accuracy of the predicted contact surface, particularly for large helix angles.

2.4. Position vector of the contact surfaces

The first step in the calculation procedure is to define the position vectors of the inner and outer contact points. The position vector of an arbitrary point $\mathrm{Q}(x_k, y_k)$ within the inner and outer contact surface written in the absolute coordinate system, is calculated as:

$$\mathbf{r}^0_{o'k} = \mathbf{r}^0_{o'o} + [\mathbf{A}^{10}][\mathbf{A}^{21}][\mathbf{A}^{3_k 2}]\mathbf{r}^{3_k}_{ok} \quad (k = i, o) \tag{11}$$

where $\mathbf{r}^0_{o'o}$ is the position vector from the origin point o' to the centre of the ball o, and $\mathbf{r}^{3_k}_{ok}$ is the position vector from the centre of the ball to the arbitrary point on the inner and outer contact surfaces. For simplicity, the latter vector is defined in the contact coordinate system and then transformed using the transformation matrices. The vectors, $\mathbf{r}^0_{o'o}$ and $\mathbf{r}^{3_k}_{ok}$ are respectively defined as:

$$\mathbf{r}^0_{o'o} = \left\{ \begin{array}{c} r_m \cos\theta \\ r_m \sin\theta \\ \theta\,(L/2\pi) \end{array} \right\}_0 \tag{12}$$

$$\mathbf{r}^{3_k}_{ok} = \left\{ \begin{array}{c} x_k \\ y_k \\ -S_k \end{array} \right\}_{3_k} \quad (k = i, o) \tag{13}$$

where, $L = 2\pi\, r_m \tan\psi$ is the pitch of the helix. S_k defines the distance from the centre of the ball to a given point on the deformed surface and is calculated as [31]:

$$S_k = \left(R_k^2 - y_k^2\right)^{1/2} - \left(R_k^2 - a_{H,k}^2\right)^{1/2} + \left((D/2)^2 - a_{H,k}^2\right)^{1/2} \quad (k = i, o) \tag{14}$$

In the latter equation, $a_{H,k}$ is the semi-major axis of the contact ellipse defined in Eq. (4), and R_k is the radius of curvature of the deformed pressure surface, which is defined as [31]:

$$R_k = \frac{2r_k D}{2r_k + D} \quad (k = i, o) \tag{15}$$

where r_k represents the raceway curvature radius. By rearranging Eqs. (11)–(15), the position vectors of the inner and outer contact surfaces are calculated:

$$\mathbf{r}_{o'k}^{0} = \left\{ \begin{array}{c} r_m \cos\theta \mp x_k (\cos\psi \sin\theta) + y_k (-\sin\alpha_k \cos\theta + \cos\alpha_k \sin\psi \sin\theta) \mp S_k (\cos\alpha_k \cos\theta + \sin\alpha_k \sin\psi \sin\theta) \\ r_m \sin\theta \pm x_k (\cos\psi \cos\theta) - y_k (\sin\alpha_k \sin\theta + \cos\alpha_k \sin\psi \cos\theta) \mp S_k (\cos\alpha_k \sin\theta - \sin\alpha_k \sin\psi \cos\theta) \\ \theta\, L/2\pi \pm x_k \sin\psi + y_k \cos\alpha_k \cos\psi \mp S_k \sin\alpha_k \cos\psi \end{array} \right\}_0 \quad (k = i, o) \tag{16}$$

2.5. Velocity analysis

The sliding speed components at an arbitrary point $\mathrm{Q}(x_k, y_k)$ on the inner and outer contact surface are determined by the difference between the absolute velocity of the ball and that of the raceway. This relationship, including an schematic representation of the theoretical calculation procedure, is illustrated in Fig. 2. The general expression for the sliding speed at the inner and outer contacts is given by:

$$\mathbf{v}_{so}^{3_o} = \mathbf{v}_{ball,o}^{3_o} - \mathbf{v}_{nut}^{3_o} \tag{17}$$

$$\mathbf{v}_{si}^{3_i} = \mathbf{v}_{ball,i}^{3_i} - \mathbf{v}_{screw}^{3_i} \tag{18}$$

where $\boldsymbol{\nu}_{\mathrm{ball},k}^{3_k}$, $\boldsymbol{\nu}_{\mathrm{screw}}^{3_k}$, and $\boldsymbol{\nu}_{\mathrm{nut}}^{3_k}$ represent the absolute velocity profiles of the ball, screw, and nut, respectively.

2.5.1. Velocity of the nut

In ball screw mechanisms, when the screw rotates an angle θ, the nut translates a linear distance $-\theta\,(L/2\pi)$ along the Z-axis in the absolute reference system. Assuming that the time derivate of θ is the angular velocity of the screw ($\mathrm{d}\theta/\mathrm{d}t = \omega$), the sliding velocity profile generated at the outer contact contact surface is [17]:

$$\mathbf{v}_{nut}^{3_o} = \omega \left\{ \begin{array}{c} (L/2\pi) \sin\psi \\ -(L/2\pi) \cos\alpha_o \cos\psi \\ (L/2\pi) \sin\alpha_o \cos\psi \end{array} \right\}_{3_o} \tag{19}$$

Note that the velocity component does not depend on the coordinate x and y of the contact surface. Since the nut undergoes purely linear motion without rotation, every point within the contact area shares the same velocity.

2.5.2. Velocity of the screw

The velocity of any point on the screw surface is obtained by differentiating its position vector with respect to time, as introduced in Eq. (16). Although the screw features a helical groove, it undergoes pure rotational motion about its axis and does not translate axially. Consequently, the Z-component of the position vector, which contains the term $\theta, L/2\pi$, does not contribute to the velocity and is therefore excluded from the derivation. To reflect this, a modified position vector $\boldsymbol{r}_{o's}$ is defined. In this position vector, that time derivate of θ is the angular velocity of the screw ($\mathrm{d}\theta/\mathrm{d}t = \omega$). In such case, the velocity of an arbitrary point on the contact surface of the screw in the contact coordinate system is [17]:

$$\mathbf{v}_{screw}^{3_i} = [\mathbf{A}^{23_i}]\,[\mathbf{A}^{12}]\,[\mathbf{A}^{01}]\frac{\mathrm{d}\boldsymbol{r}_{o's}^{0}}{\mathrm{d}t} \tag{20}$$

$$\mathbf{v}_{screw}^{3_i} = \omega \left\{ \begin{array}{c} (r_m - S_i \cos\alpha_i) \cos\psi - y_i \cos\psi \sin\alpha_i \\ (S_i - r_m \cos\alpha_i) \sin\psi + x_i \cos\psi \sin\alpha_i \\ -r_m \sin\alpha_i \sin\psi - x_i \cos\psi \cos\alpha_i + y_i \sin\psi \end{array} \right\}_{3_i} \tag{21}$$

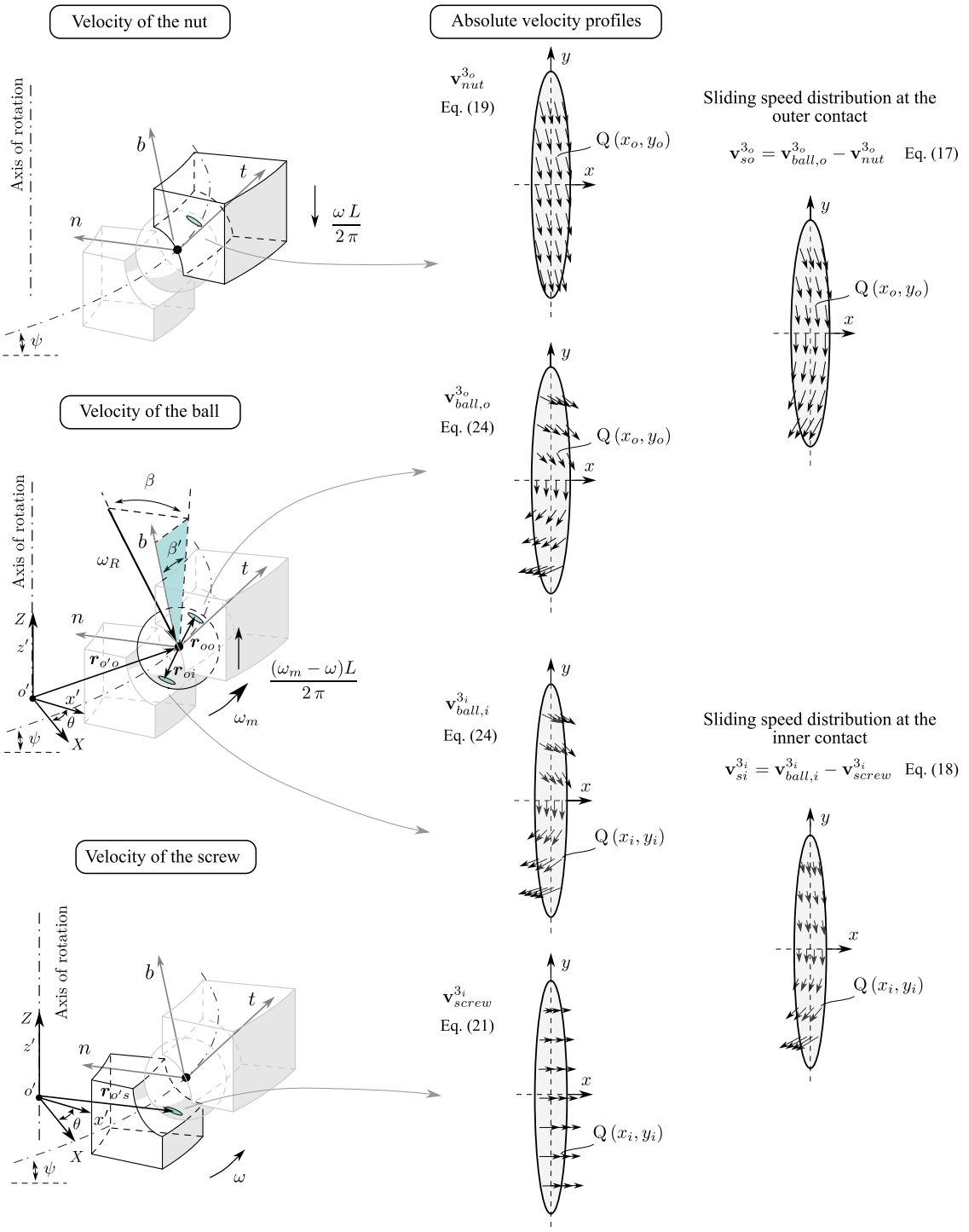

Fig. 2. Schematic representation of the theoretical calculation procedure of the inner and outer contact kinematics in ball screws.

2.5.3. Velocity of the ball

The overall motion of the ball relative to the raceways is composed by two primary components, as shown in Fig. 2. First, the ball moves along the helical path of the raceways, which is described by the orbital angular velocity ω_m. Second, the ball simultaneously rotates about its own axis with an angular velocity ω_R. The orbital and rotational velocities are calculated using the analytical expressions proposed in [55], which include the effect of the translational velocity component in contrast to other expressions found in the scientific literature:

$$\omega_m = \omega\left(1 + \frac{r_i'\left((r_m + r_o'\cos\alpha_o)\cos\psi + (L/2\pi)\sin\psi\right)(\cos\beta\cos\beta'\cos\alpha_i + \sin\beta\sin\alpha_i)}{r_o'\left((r_m - r_i'\cos\alpha_i)\cos\psi + (L/2\pi)\sin\psi\right)(\cos\beta\cos\beta'\cos\alpha_o + \sin\beta\sin\alpha_o)}\right)^{-1} \tag{22}$$

$$\omega_R = \omega_m\left(\frac{(r_m - r_i'\cos\alpha_i)\cos\psi + (L/2\pi)\sin\psi}{r_i'(\cos\beta\cos\beta'\cos\alpha_i + \sin\beta\sin\alpha_i)}\right) \tag{23}$$

The absolute velocity profile of the ball at the contact interface results from the sum of the translational motion and the rotational velocity of the ball, calculated as:

$$\mathbf{v}_{ball,k}^{3_k} = \mathbf{v}_{b1,k}^{3_k} + \mathbf{v}_{b2,k}^{3_k} \quad (k = i, o) \tag{24}$$

where, $\mathbf{v}_{b1}$ is the velocity profile generated by the orbital translation motion and $\mathbf{v}_{b2}$ is the velocity profile related to the rotation of the ball around its own axis. These two components are calculated separately in the following subsections.

Translational velocity of the ball

The velocity component at the contact surface generated by the translational motion of the ball is calculated by the time derivative of its position vector. A key difference between the present formulation and the traditional formulation in the literature [17] lies in how this position vector is defined. In the conventional formulation, the velocity is computed by differentiating the position vector of the ball centre. This is described with the first term in Eq. (25). However, since we are analysing the sliding speed at the contact interface, the position vector must extend to the contact point (see Fig. 2). As a result, the additional term representing the offset from the ball centre to the contact surface must be included in the calculation:

$$\mathbf{v}_{b1,k}^{3_k} = \frac{\mathrm{d}\left(\mathbf{r}_{o'o} + \mathbf{r}_{ok}\right)}{\mathrm{d}t} = \frac{\mathrm{d}\mathbf{r}_{o'o}}{\mathrm{d}t} + \frac{\mathrm{d}\mathbf{r}_{ok}}{\mathrm{d}t} \quad (k = i, o) \tag{25}$$

Assuming that the time derivate of the angular displacement of the ball is $\mathrm{d}\theta/\mathrm{d}t = \omega_m$. When the two terms are included, the velocity at the contact point becomes:

$$\mathbf{v}_{b1,k}^{3k} = \begin{Bmatrix} \pm(\omega_m - \omega)\frac{r_m}{\cos\psi} \pm \omega r_m\cos\psi \\ -\omega r_m\cos\alpha_k\sin\psi \\ \mp\omega r_m\sin\alpha_k\sin\psi \end{Bmatrix}_{3_k} + \underbrace{\omega_m\begin{Bmatrix} -S_k\cos\alpha_k\cos\psi \mp y_k\sin\alpha_k\cos\psi \\ \pm S_k\sin\psi \pm x_k\sin\alpha_k\cos\psi \\ \mp x_k\cos\psi\cos\alpha_k \pm y_k\sin\psi \end{Bmatrix}_{3_k}}_{\text{Missing term in the literature formulation}} \quad (k = i, o) \tag{26}$$

where the second term is that representing the offset from the ball centre to the contact surface. This has not been considered in the previous literature works. As demonstrated in the results, including this additional term significantly affects the sliding speed distribution within the contact surface and provides a new framework to describe contact kinematics.

Velocity of the ball around its own axis

As illustrated in Fig. 2, the rotational velocity of the ball around its own axis ω_R, written in the Frenet-Serret coordinate system is [18]:

$$\boldsymbol{\omega}_b^2 = \begin{Bmatrix} \omega_t \\ \omega_n \\ \omega_b \end{Bmatrix}_2 = \begin{Bmatrix} \omega_R\cos\beta\sin\beta' \\ -\omega_R\sin\beta \\ -\omega_R\cos\beta\cos\beta' \end{Bmatrix}_2 \tag{27}$$

where β and β' represent the pitch and yaw angles of the ball, respectively. These two angles define the rotation axis of the ball in the Frenet-Serret coordinate system. It should be emphasised that some authors use the pitch angle (β) to denote the helix angle (ψ). However, for clarity and consistency, in this work the term helix angle refers to the screw geometry, whereas the pitch angle refers to the orientation of the ball's rotational axis (see Fig. 2).

The velocity at an arbitrary point Q (x_k, y_k) on the ball surface is given by the cross product of the angular velocity vector and the position vector from the ball centre [18,73]:

$$\mathbf{v}_{b2,k}^{3k} = [\boldsymbol{A}^{23_k}]\,\boldsymbol{\omega}_b^2 \times \boldsymbol{r}_{ok}^{3_k} \quad (k = i, o) \tag{28}$$

Expanding the expression yields:

$$\mathbf{v}_{b2,k}^{3k} = \begin{Bmatrix} -S_k(\omega_n\sin\alpha_k + \omega_b\cos\alpha_k) \pm y_k(\omega_n\cos\alpha_k - \omega_b\sin\alpha_k) \\ \pm S_k\omega_t \mp x_k(\omega_n\cos\alpha_k - \omega_b\sin\alpha_k) \\ \pm y_k\omega_t - x_k(\omega_n\sin\alpha_k + \omega_b\cos\alpha_k) \end{Bmatrix}_{3_k} \quad (k = i, o) \tag{29}$$

2.6. Sliding speed composition at the contact interface

The formulation and resulting equations for calculating the sliding speed distribution of the contact introduced in the previous section in Eqs. (17) and (18) are extensive and may be challenging to interpret. To improve clarity and support understanding, this section breaks down the sliding speed into its fundamental components. This provides physical insight into the nature of kinematics in ball screw contacts. The sliding speed distribution can be described as the combination of three distinct components: rolling slip ($\boldsymbol{v}_{\mathrm{roll},k}$), side slip ($\boldsymbol{v}_{\mathrm{side},k}$), and spinning slip ($\boldsymbol{v}_{\mathrm{sp},k}$). As shown in the following expression, each component contributes in a specific direction within the local contact coordinate system:

$$\mathbf{v}_{sk}^{3_k} = \underbrace{\begin{Bmatrix} v_{\mathrm{roll,k}} \\ 0 \\ 0 \end{Bmatrix}}_{\text{Rolling}} + \underbrace{\begin{Bmatrix} 0 \\ v_{\mathrm{side,k}} \\ 0 \end{Bmatrix}}_{\text{Side}} + \underbrace{\begin{Bmatrix} v_{\mathrm{sp},k} \\ v_{\mathrm{sp},k} \\ 0 \end{Bmatrix}}_{\text{Spinning}} \quad (k = i, o) \tag{30}$$

Each of these sliding components is illustrated in Fig. 3 and is described in detail in the following paragraphs.

- **Rolling slip:** The rolling slip is generated by the velocity components resulting from the projection of the rotational speed vectors onto the y axis of the contact coordinate system. The sliding vectors are aligned in the rolling direction of the ball. This slip arises from the curvature of the deformed contact surfaces, defined by the harmonic mean profile of the ball and the raceway, which is described with the variable S_k in Eq. (14). As the ball rotates, surface points located at different distances from the axis of rotation exhibit varying linear velocities. This variation produces a parabolic velocity distribution across the contact interface. As a result, rolling slip is always present in rolling element contacts [31].

  The variations in tangential velocity components through the x-axis, leads to exist specific locations where the ball and raceway surfaces have the same tangential velocity, known as pure rolling points. When the contact is uniquely composed by rolling slip, these points are symmetrically positioned with respect to the x-axis (as illustrated in Fig. 3). However, in ball screw mechanisms, where side and spinning components coexist, these points are displaced or may even fall outside the contact ellipse. The equation of the rolling slip distribution reads:

$$v_{roll,k} = \omega_k \left(\frac{r_m}{\cos\psi} \mp S_k \cos\alpha_k \cos\psi \right) - S_k \left(\omega_n \sin\alpha_k + \omega_b \cos\alpha_k\right) \quad (k = i, o) \tag{31}$$

  where, $\omega_i = \omega_m - \omega$ and $\omega_o = -\omega_m$. This criteria is maintained for all the equations below.
- **Side slip:** The side slip is a distinctive feature in the contact kinematics of ball screws, caused by the velocity components resulting from the projection of rotational speed vectors onto the x-axis of the contact coordinate system. Side slip in ball screws occurs uniquely in the transverse direction of the contact and arises from the helical path the ball follows. The velocity profile is the same for each point along the semi-minor axis.

$$v_{\mathrm{side},k} = \omega_k S_k \sin\psi \pm \omega_t S_k \quad (k = i, o) \tag{32}$$

- **Spinning slip:** Spinning slip arises from the projection of rotational speeds along the z-axis of the contact and it is commonly described in the literature by the spinning speed (ω_{sp}). This motion generates slip in both the rolling and transverse directions,

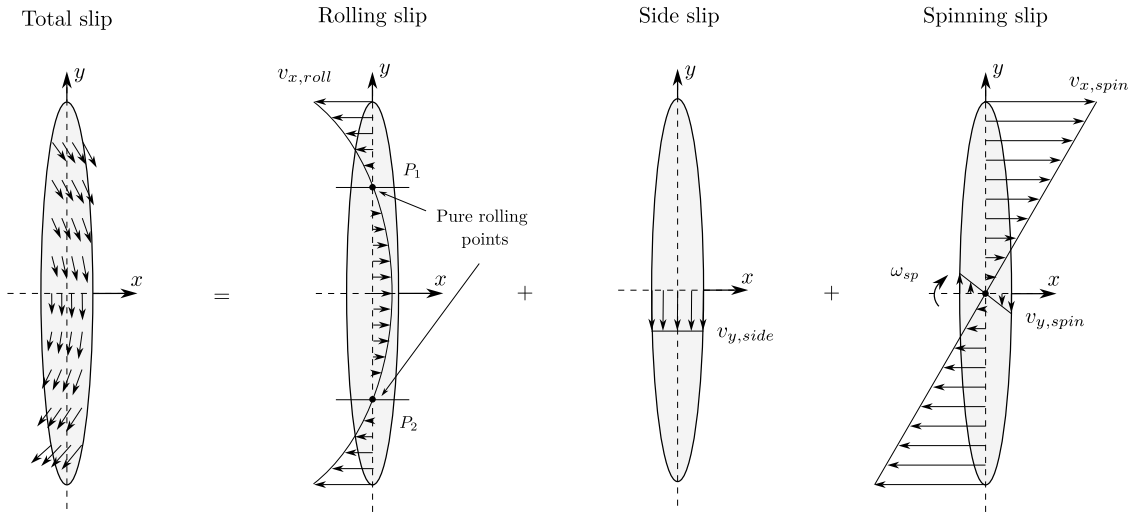

Fig. 3. Independent effect of the rolling, side and spinning slips on the total sliding speed distribution.

influencing the overall contact pattern. The expression related to the spinning slip component is defined as:

$$v_{x,sp} = -\omega_{sp,k}\, y_k, \qquad v_{y,sp} = \omega_{sp,k}\, x_k \quad (k = i, o) \tag{33}$$

being, x_k and y_k the coordinates of the arbitrary Q point within the contact surface, and $\omega_{sp,k}$ the spinning speed of the contact:

$$\omega_{sp,k} = \omega_k \cos\psi \sin\alpha_k \mp (\omega_n \cos\alpha_k - \omega_b \sin\alpha_k) \quad (k = i, o) \tag{34}$$

2.7. Definition of entrainment speed and three parameter SRR framework

The complexity of the sliding speed distribution in ball screw contacts makes the slide-to-roll ratio (*SRR*) insufficient for fully capturing and quantifying the contact kinematics. To address this limitation, this section introduces a new three parameter approach to characterise the multidirectional contact behaviour observed at ball-screw interfaces.

As described in the previous section, each point on the contact surface has a specific sliding speed component. Hence, each point of the contact surface exhibits a different sliding speed. Literature addressing similar sliding speed distributions in other mechanical systems solves this issue by calculating the parameters at the centre of the contact ellipse [64,66–68]. In this work the same strategy is followed, and therefore the variables are evaluated at centre of the ellipse being the coordinates $x_k = 0$ and $y_k = 0$ (see Fig. 4).

2.7.1. Entrainment speed

The entrainment speed is defined as the mean rolling speed of the contacting bodies and is calculated as:

$$\mathbf{v}_{e,k} = \frac{\mathbf{v}_{ball,k} + \mathbf{v}_{screw/nut}}{2} \quad (k = i, o) \tag{35}$$

$$\mathbf{v}_{e.k}^{3_k} = \frac{1}{2}\left\{ \begin{array}{c} \omega_k \left(\frac{r_m}{\cos\psi} \mp S_k \cos\alpha_k \cos\psi\right) + S_k\,(\omega_n \sin\alpha_k + \omega_b \cos\alpha_k) \\ \omega_k\, S_k \sin\psi \mp \omega_t\, S_k \\ 0 \end{array} \right\}_{3k} \quad (k = i, o) \tag{36}$$

As shown in Fig. 4, the absolute velocity components of the ball and the screw are not aligned with the rolling direction. Therefore, the entrainment speed is not necessarily oriented in the rolling direction of the ball. The angle of the vector formed by the entrainment speed and the rolling direction x is given by:

$$\gamma_{,k} = \tan^{-1}\left(\frac{v_{e,y}}{v_{e,x}}\right) \quad (k = i, o) \tag{37}$$

2.7.2. Slide-to-roll ratio

The slide-to-roll ratio (*SRR*) quantifies the relationship between the sliding speed and the entrainment speed at the contact interface. Following the standard definition in the literature, it is calculated as:

$$SRR_k = \frac{|\boldsymbol{v}_{s,k}|}{|\boldsymbol{v}_{e,k}|} \quad (k = i, o) \tag{38}$$

where $\boldsymbol{v}_s$ is the sliding speed vector defined in Eq. (30), and $\boldsymbol{v}_e$ is the entrainment velocity at the contact.

Fig. 4 illustrates that the *SRR* vector is generally not aligned with the x-axis due to the combined effects of rolling, side, and spinning slip. To fully characterise the *SRR*, its orientation must also be defined. For that, the angle ϕ between the *SRR* vector and the x-axis is determined using the following trigonometric relation:

$$\phi_k = \tan^{-1}\left(\frac{v_{s,y}}{v_{s,x}}\right) \quad (k = i, o) \tag{39}$$

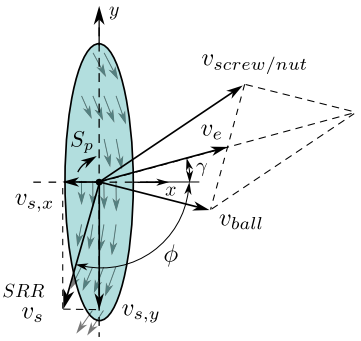

Fig. 4. Representation of the components of the proposed *SRR* framework.

2.7.3. Spin-to-roll ratio

The *SRR*s are calculated at the centre of the contact ellipse, where the effect of spinning slip is zero. However, spinning slip still influences the overall sliding speed distribution across the contact. Therefore, an additional parameter is required to quantify the spinning component. For this purpose, the spin-to-roll ratio is employed, a parameter commonly employed in other mechanical systems where spin has a substantial role [68]:

$$S_{p,k} = \frac{\omega_{sp,k}\sqrt{a_{H,k}\, b_{H,k}}}{|v_{e,k}|} \quad (k = i, o) \tag{40}$$

being, a_H and b_H the semi-major and minor axis of the contact ellipse, respectively.

By utilizing these three variables, the contact kinematics can be fully characterized, ensuring a comprehensive understanding of the sliding speed distribution. This approach eliminates ambiguity and provides a clear framework for analysing the motion within the contact interface, simplifying the problem by reducing it to only three parameters.

2.8. Solution procedure

The proposed formulation describes the contact kinematics of a ball on the basis of a specific load state and global motion. This state is fully determined by a set of variables: the contact loads (W_k), the contact angles (α_k), the pure rolling radii (r'_k), the yaw angle (β'), and the pitch angle (β). These can be grouped into two categories: load-related variables (W_k and α_k) and motion-related variables (r'_k, β', and β). The contact kinematic is determined once these variables are known.

The values of the variables depend on the component geometry, material properties, lubrication regime, and operating conditions of the target application. Determining them requires analysing the equilibrium of forces and moments acting on each ball. Fig. 5 presents the workflow of commonly employed procedures in the literature to calculate these input variables. The figure also shows how these inputs are introduced in the proposed formulation to calculate contact kinematics. Depending on the application and author, different methods are selected to calculate the these input variables. The objective of this section is to describe the inclusion of the proposed contact kinematic formulation, in any of these solving strategies. The detailed equations of each procedure to calculate the input variables are omitted here, as they are extensively documented in the literature, as shown later in this section. The main conceptual aspects of the procedure, particularly those most relevant to the subsequent analysis and discussion, are briefly summarised below.

The solution procedure is as follows:

- **Load and absolute velocity of the ball:** The load state and absolute motion are typically calculated using quasi-static or dynamic models, widely documented in the literature of ball bearings and ball screws [35,43,74,75]. In these models the variables to determine the load and motion of the ball are calculated as follows:
  - **Contact load and angle** (W_k, α_k): Derived from analytical formulations based on elastic deformation and equilibrium equations, which consider centrifugal forces (F_c) and gyroscopic moments (M_g) [18,43].
  - **Kinematic constraints (r'_k, β', β):** The degrees of freedom of the ball are mathematically constrained by r'_k, β', and β. The pure rolling radius defines the radial position of zero slip in the rolling direction, while the yaw and pitch angles set the orientation of the rotational axis of the ball. These parameters strongly influence the sliding speed distribution and are sensitive to operational conditions [18,76]. Several strategies exist in the literature to calculate these variables. All methods assume the pure rolling radii to be equal the radius of the ball and the yaw angle to be 0, resulting in distinct formulations for predicting the pitch angle. The available approaches for computing the pitch angle are the following:
    - **Constant pitch angle approximation (CONST):** Assumes β equal to the nominal contact angle, independently of the operating conditions [29,43].
    - **Inner Raceway Control hypothesis (IRC):** Sets the pitch angle such that the spinning speed at the outer contact is zero. [33,34,49,77].
    - **Outer Raceway Control hypothesis (ORC):** Determines the pitch angle value that eliminates the spinning speed at the inner contact [33,34,49,77].
    - **Iterative formulation (ITE):** Proposed by Wei and Lin [18], this method computes the pitch angle through an iterative procedure rather than a single analytical expression.
    - **Geometric relation (GEO):** Computes the pitch angle as the average of the inner and outer contact angles [78].
    - **Relation based on D'Alembert's hypothesis (DAL):** Predicts the pitch angle using D'Alembert's inertia principle, assuming that the total power associated with all forces acting on the ball is zero [79].

    The assumptions and governing equations associated with each method are summarised in Table 1. The last two approaches (GEO and DAL), originally developed for ball bearing applications, have been incorporated in this study to provide a more comprehensive framework for analysing contact kinematics. All existing methods determine the kinematic constraints as functions of the contact angles and loads, but none explicitly account for friction-related effects such as lubricant properties. It should also be noted that no consensus currently exists in the literature regarding the most appropriate approach.
  - **Orbital and rotational speeds (ω_m, ω_R):** Once the kinematic constraints are defined, the orbital (ω_m) and rotational (ω_R) speeds of the ball are calculated using Eqs. (22)-(23), redefined by the authors in [55].

  Under certain operating conditions, inertial effects, such as centrifugal forces and gyroscopic moments, can modify the contact loads and contact angles [5,18]. For this reason, some models adopt an iterative solution procedure to achieve equilibrium among

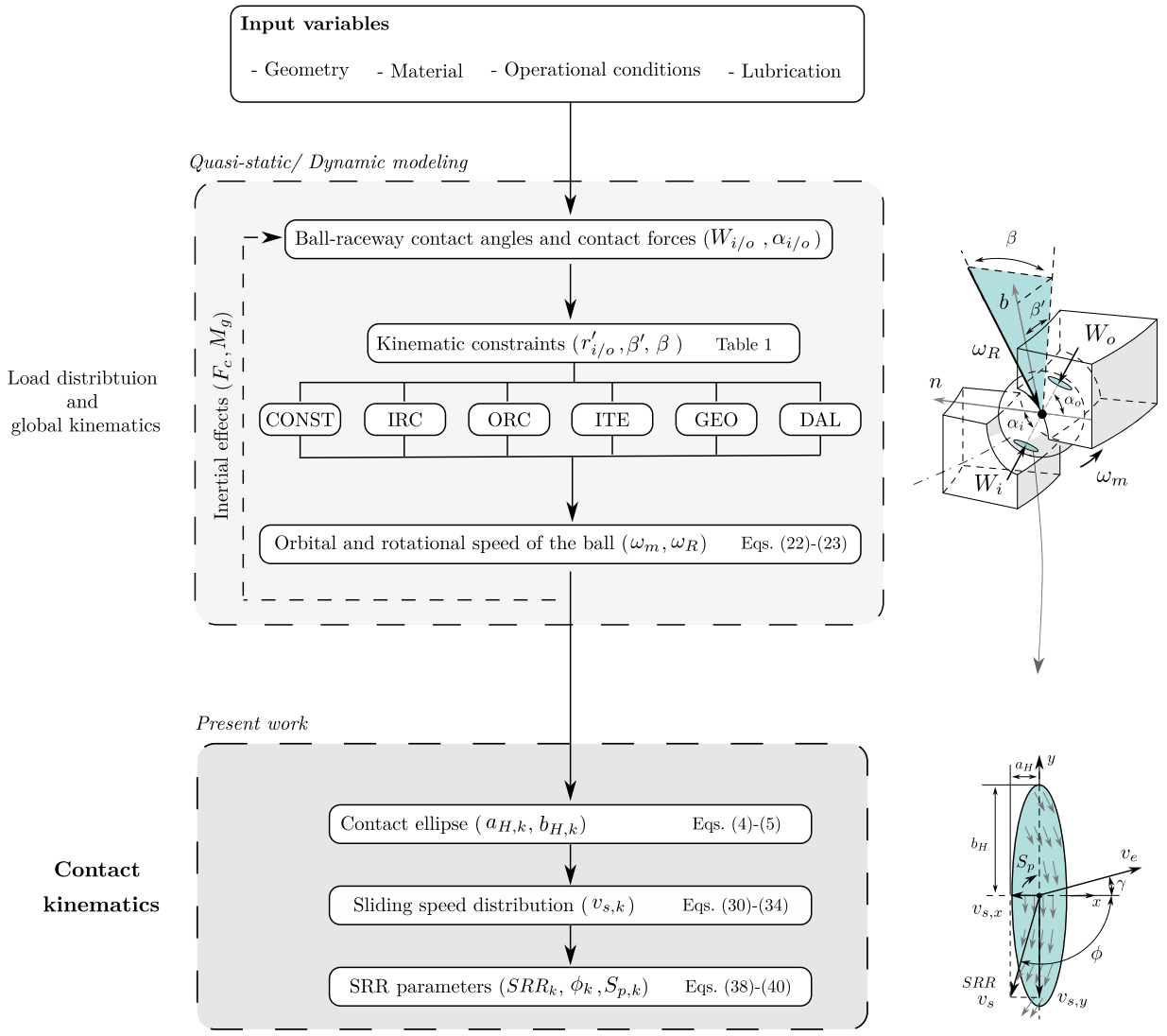

Fig. 5. Flowchart of the computational procedure to determine contact kinematics.

the interacting variables. The changes produced by these inertial effects directly affect the equations defining the kinematic constraints listed in Table 1, thereby influencing the resulting sliding-speed distribution.

It should be noted that the methods for calculating the kinematic constraints have negligible effect on the orbital and rotational speed of the ball, and therefore their values have minor effect on the load state of the ball. Nevertheless, as demonstrated in the following sections, they have a governing impact on contact kinematics.

Table 1
Summary of the literature approaches to calculate the kinematic constraints.

Method	Pure rolling radii	Yaw angle	Pitch angle
CONST	$r' = D/2$	$\beta' = 0$	$\beta = \alpha^0$
IRC	$r' = D/2$	$\beta' = 0$	$\beta = \text{atan}\left(\frac{\sin\alpha_i}{\cos\alpha_i - (D/d_m)}\right)$
ORC	$r' = D/2$	$\beta' = 0$	$\beta = \text{atan}\left(\frac{\sin\alpha_o}{\cos\alpha_o + (D/d_m)}\right)$
ITE	$r' = D/2$	$\beta' = 0$	$\beta \longrightarrow$ Iterations
GEO	$r' = D/2$	$\beta' = 0$	$\beta = (\alpha_i + \alpha_o)/2$
DAL	$r' = D/2$	$\beta' = 0$	$\beta = \text{atan}\left(\frac{C(B+1)\sin\alpha_i + 2\sin\alpha_o}{C(B+1)\cos\alpha_i + 2(\cos\alpha_o + \gamma') + \gamma' C(\cos(\alpha_i - \alpha_o) - B)}\right)$, with $C = \frac{W_o}{W_i}\frac{a_{H,o}}{a_{H,i}}\frac{L_2(k_{e,o})}{L_2(k_{e,i})}$, $B = \frac{1+\gamma'\cos\alpha_o}{1-\gamma'\cos\alpha_i}$ and $\gamma' = D/d_m$

- **Contact kinematics:** After determining the load state and absolute velocity of the ball, the contact kinematic formulation presented in this work is applied to compute the sliding speed distribution at the contact interface.
  - **Contact ellipse ($a_{H,k}$, $b_{H,k}$):** The semi-major and semi-minor axes of the contact ellipse ($a_{H,k}$, $b_{H,k}$) are calculated using Eqs. (4)-(5). In this work, the formulation of Bertolino et al. [71,72] is employed to calculate the principal groove profiles using the Eqs. (9)-(10)
  - **Sliding speed distribution ($v_{s,k}$):** The sliding speed distribution $v_{s,k}$ is calculated as the sum of rolling slip, side slip, and spinning slip components from Eqs. (30)–(34).
  - ***SRR* parameters (SRR_k, ϕ_k, $S_{p,k}$):** Once the sliding speed distribution is determined, the quantifying parameters -entrainment speed (v_e), entrainment angle (γ), slide-to-roll ratio (SRR), SRR angle (ϕ), and spin-to-roll ratio (S_p)-are calculated using Eqs. (35)-(40).

3. Definition of the case studies

All simulations are performed using the same reference ball screw. Table 2 summarises the main parameters of the reference configuration, which corresponds to a single-nut, single-arc raceway ball-screw design. For the analysis of the results, the contact load and contact angles are calculated using the analytical elastic deformation and equilibrium equations proposed in [18,43].

Three analyses were performed: two case studies and one comparative discussion. Their objectives and specifications are detailed below and summarised in Table 3:

- **Case 1:** A comparison is conducted between the contact kinematic characteristics predicted by the revised formulation proposed in this work and those obtained using the traditional formulation [17]. This analysis was performed at $F_a = 1500$ N and $\omega = 1000$ rpm, resulting in contact loads of $W_{i/o} = 151$ N and contact angles of $\alpha_{i/o} = 41°$. The simulations in this case study are performed following the CONST approach introduced in Section 2.8 and summarised in Table 1.

  The analysis spans helix angle of the reference geometry from 0° to 40°, taking as a reference ranges of commercially available ball screw geometries [80–84]. To highlight the implications of the revised formulation, two specific configurations are examined in detail. First, a ball bearing geometry was used to validate the proposed formulation against well-known and widely accepted contact kinematic models. Since a ball bearing is a specific type of ball screw with zero pitch, the helix angle in this configuration was set to 0°. Second, the comparison was extended to a ball screw geometry to evaluate the influence of the corrected formulation under ball screw geometries. In this instance, the helix angle was set to 10°.
- **Case 2:** A parametric analysis to evaluate the influence of key kinematic constraints-the pure rolling radius (r'), yaw angle (β'), and pitch angle (β)-on the contact kinematics. The simulation is conducted under an axial load of $F_a = 1500$ N and a rotational speed of $\omega = 1000$ rpm, leading to contact loads of $W_{i/o} = 151$ N and contact angles of $\alpha_{i/o} = 41°$.

  To assess the individual effect of each constraint, they were varied independently while keeping the remaining two fixed. This approach enables a clear and isolated evaluation of their impact on contact kinematics. The analysed parameter ranges and the selected reference values are summarised in Table 4, and listed below:

Table 2
Geometry and material characteristics of the analysed ball screw.

Parameter	Value
Ball diameter, D [mm]	7.94
Pitch diameter, d_m [mm]	38.5
Raceway curvature radius, $r_{i/o}$ [mm]	4.2
Ball-raceway nominal contact angle, α^0 [°]	40
Helix angle, ψ [°]	10
Pitch, L [mm]	21.3
Turns, [-]	1
Number of balls, Z [-]	15
Material	AISI 52100
Young's modulus, E [GPa]	210
Poisson's ratio, ν [-]	0.3
Density, ρ [kg/m^3]	7850

Table 3
Summary of the case studies.

	Objective	Operating conditions	Constraint method
Case 1	Validation of the proposed model	$F_a = 1500$ N $\omega = 1000$ rpm	CONST
Case 2	Parametric study of the kinematic constraints	$F_a = 1500$ N $\omega = 1000$ rpm	–
Discussion	Comparison of different methods under varying operating conditions	$F_a = 500–3000$ N $\omega = 1000$ and 3500 rpm	CONST, IRC, ORC, ITE, GEO, DAL

Table 4
Summary of the parametric analysis ranges and selected cases for detailed evaluation in Case 2.

Parameter	Fixed values	Analysed range	Selected values
Pure rolling radius r' [mm]	3.97	3.92 – 4.02	3.95, 3.97, 3.99
Yaw angle β' [°]	1	−3 – 3	0, 1, 2
Pitch angle β [°]	40	28 – 52	34.3, 40, 44, 50.1

(a) Pure rolling radius (r'): The reference value was set to radius of the ball ($r' = D/2$), corresponding to 3.97 mm, consistent with values reported in the literature. The parameter was varied by ±0.05 mm around this reference value. Within this range, three representative values of 3.95 mm, 3.97 mm and 3.99 mm, were selected for detailed analysis.
(b) Yaw angle (β'): The yaw angle β' is consistently assumed to be 0° in the literature. However, this value is not the most suitable reference for the parametric study, because it neglects the influence of β on the side slip component. To ensure a correct numerical sensitivity, a reference value of 1° was adopted and the parameter was varied within ±3°. Three representative values-0°, 1°, and 2°-were examined in detail.
(c) Pitch angle (β): For the parametric study, the reference value was set to 40° and analysed within a range of ±12°, covering the values predicted by the approaches presented in Table 1. Within this range, four representative pitch-angle values were selected to analyse how variations in β influence the contact kinematics. To enhance the practicality and clarity of the analysis, these representative values correspond to the following literature approaches: CONST with $\beta = 40°$, IRC with $\beta = 50.1°$, ORC with $\beta = 34.3°$, and ITE with $\beta = 44°$.

- **Discussion:** An analysis is conducted to evaluate the effect of operational conditions on contact kinematics. The axial load was varied from 500 N to 3500 N, while two rotational speeds of 1000 rpm and 3500 rpm are evaluated. To provide a comprehensive overview of contact kinematics, simulations are performed using all the approaches presented in Table 1 (Section 2.8) and compared accordingly.

4. Results

4.1. Comparison of the literature and revised contact kinematic formulations

To evaluate the differences between the traditional and revised contact kinematic formulations, Fig. 6 presents a comparison of several variables-entrainment speed, sliding velocity components, and spinning speed-computed across a range of helix angles.

Angular contact ball bearing ($\psi = 0°$)

When the helix angle is set to zero ($\psi = 0°$), the ball screw geometry reduces to an angular contact ball bearing. Under this limiting condition, the kinematic behaviour should coincide with the well-established ball bearing formulation [31]. As shown in Fig. 6, the revised formulation accurately reproduces the reference ball bearing results. In contrast, the traditional formulation exhibits significant deviations from the ball bearing predictions. The most notable discrepancies arise in the entrainment speed (v_e), which is underestimated, and in the x-component of the sliding speed velocity (v_{sx}), which is predicted to be excessively high. Such values are unrealistic for rolling-element contacts.

A more detailed comparison is shown in Fig. 7, which illustrates the full sliding speed distribution within the contact interface for an angular contact ball bearing case. The traditional formulation predicts a velocity field aligned with the rolling direction and exhibiting unrealistically high magnitudes. This results in a unidirectional pattern that fails to capture the characteristic spiral distribution observed in bearing contacts [31,76]. Although the traditional formulation yields spinning speeds comparable to those predicted by validated ball bearing models, the overestimated x-component suppresses the relative influence of spinning in the overall distribution.

In contrast, the revised formulation reproduces the reference ball-bearing sliding-speed distribution exactly. When the helix angle is set to zero ($\psi = 0°$), the equations of the proposed formulation reduce to those of the ball bearing formulation, and the results are identical [31]. This confirms both its accuracy and the mathematical consistency of the proposed approach. Validation under this benchmark configuration provides strong evidence of the physical robustness of the corrections introduced.

Ball screw ($\psi > 0°$)

When the helix angle increases, the geometry corresponds to a conventional ball screw ($\psi > 0°$). In this regime, the discrepancies between the two formulations become more pronounced, as illustrated in Fig. 6. All evaluated parameters exhibit increasing divergence with helix angle, indicating that the assumptions in the traditional model are no longer valid for ball screw geometries.

The evolution of the semi-major (a_H) and semi-minor (b_H) axes of the contact ellipse also reveals marked differences. Although the contact load (W_k) remains identical for all helix angles, the revised formulation predicts variations in ellipse dimensions owing to the improved definition of groove curvature radii based on Bertolino *et al.*'s differential-geometry approach [71,72]. In contrast, the classical formulation yields ellipse sizes that remain constant with helix angle, thereby neglecting this geometric effect. Accurate theoretical characterisation of the contact ellipse is crucial because it directly influences the contact pressure and, consequently, all subsequent contact phenomena.

Among all plotted variables in Fig. 6, a particular case arises with the entrainment speed. Although Eq. (36) provides different expressions for the inner and outer contacts, numerical evaluation shows nearly identical values. This explains why only one line

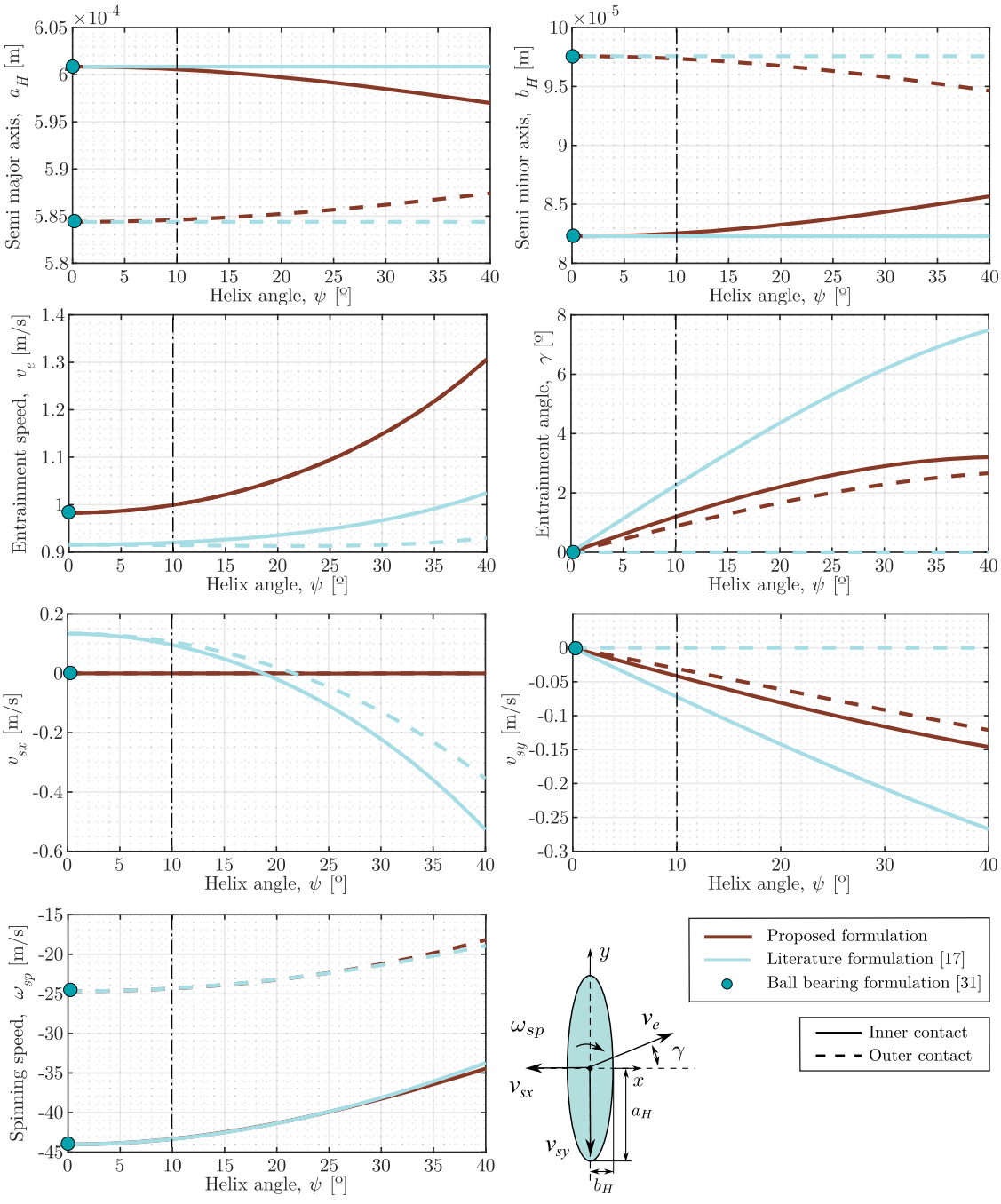

Fig. 6. Comparison of size of the contact ellipse, entrainment speed, sliding velocity components, and spinning speed across varying helix angles, for the traditional and revised contact kinematic formulations.

appears in the plot. Such convergence of entrainment velocities is well established in ball bearing analyses [85], further supporting the validity of the result.

To complete the analysis of the entrainment speed, attention must be paid to the orientation of the entrainment vectors. Although the magnitudes at both contacts are nearly identical, their orientations differ slightly. The deviation is more pronounced at the inner contact, reflecting the influence of the helical geometry on the direction of motion. In contrast, the predictions of the classical formulation deviate considerably: at the outer contact the entrainment angle remains zero, whereas at the inner contact it is almost twice as large as that obtained with the revised model.

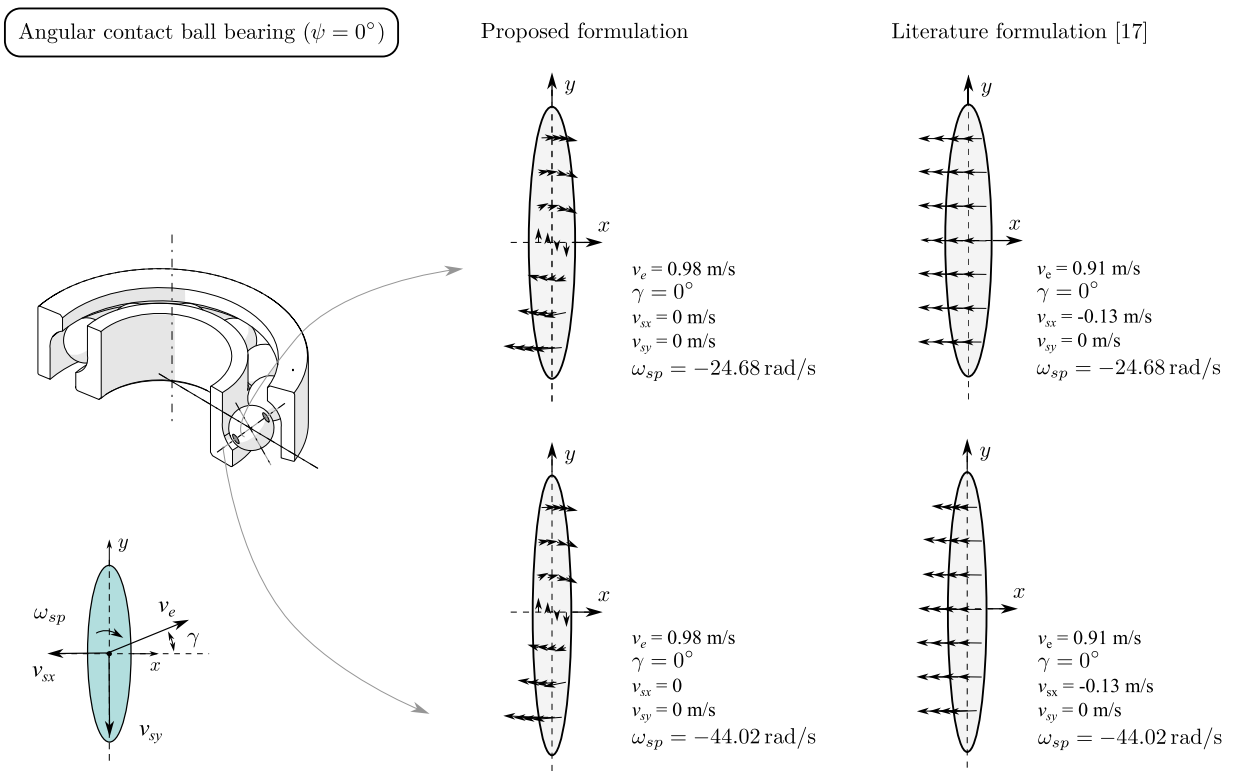

Fig. 7. Comparison of contact kinematics calculated using the literature and proposed formulations at ball bearing scale ($\psi = 0°$).

Regarding the sliding-velocity components, the discrepancies between the two formulations are substantial. The traditional formulation predicts excessively high values of v_{sx}, suggesting significant slip in the rolling direction. This is inconsistent with the fundamental rolling motion of the ball, where slip along the rolling axis should remain minimal. Similarly, the traditional model produces asymmetric side-slip magnitudes between the inner and outer contacts-one vanishing while the other is excessively large. In contrast, the revised formulation predicts balanced side-slip values at both contacts.

Concerning the spinning speed, both formulations show an increasing trend with helix angle. However, the classical formulation predicts slightly higher values at the outer contact and lower values at the inner contact. The difference increases with helix angle, indicating that even for this parameter, the revised model provides a more reliable description of the kinematics.

To further illustrate these discrepancies, Fig. 8 shows the sliding speed distributions for a specific ball screw with a helix angle of $\psi = 10°$. The traditional formulation results in a simplified pattern, with sliding vectors aligned with the x-component in both contacts. This arises from the previously mentioned high predictions in the x sliding component. In contrast, the proposed formulation yields a fundamentally different sliding speed distribution. The sliding vectors show a predominant alignment in the transverse direction, forming a spiral pattern. These two characteristics highlight the significant contributions of both side and spinning slip.

A closer inspection of the sliding velocity at the centre of the contact ellipse further emphasises the differences between the two formulations. The proposed model predicts a sliding magnitude approximately three times smaller than that of the traditional formulation. Moreover, while the traditional model assumes that sliding occurs predominantly in the x-component, this assumption is no longer valid in the result given in the revised formulation. In the revised model, the sliding direction deviates significantly from the rolling axis due to the dominant influence of side slip, which alters both the orientation and structure of the velocity field.

Regarding the spinning component, both formulations predict similar magnitudes. However, its effect on the overall sliding speed distribution becomes substantially more pronounced in the revised formulation. This is primarily due to the reduced sliding components in the rolling direction, which increase the relative contribution of spinning.

Differences are also observed in the entrainment speed. The traditional model predicts a value of 0.91 m/s, while the revised formulation yields 1.00 m/s. Additionally, the direction of the entrainment vector deviates from the rolling axis by 0.87° at the inner contact and 1.19° at the outer contact, highlighting the influence of the helical geometry on the effective contact motion.

4.2. Comparison between single SRR and the proposed three-parameter approach

Having established the differences between the two formulations, this section examines the limitations of traditional *SRR*-based quantification. As stated in the introduction, while a single Slide-to-Roll Ratio (*SRR*) may be sufficient to describe contact kinematics in certain machine elements, its applicability to ball screw mechanisms requires careful validation.

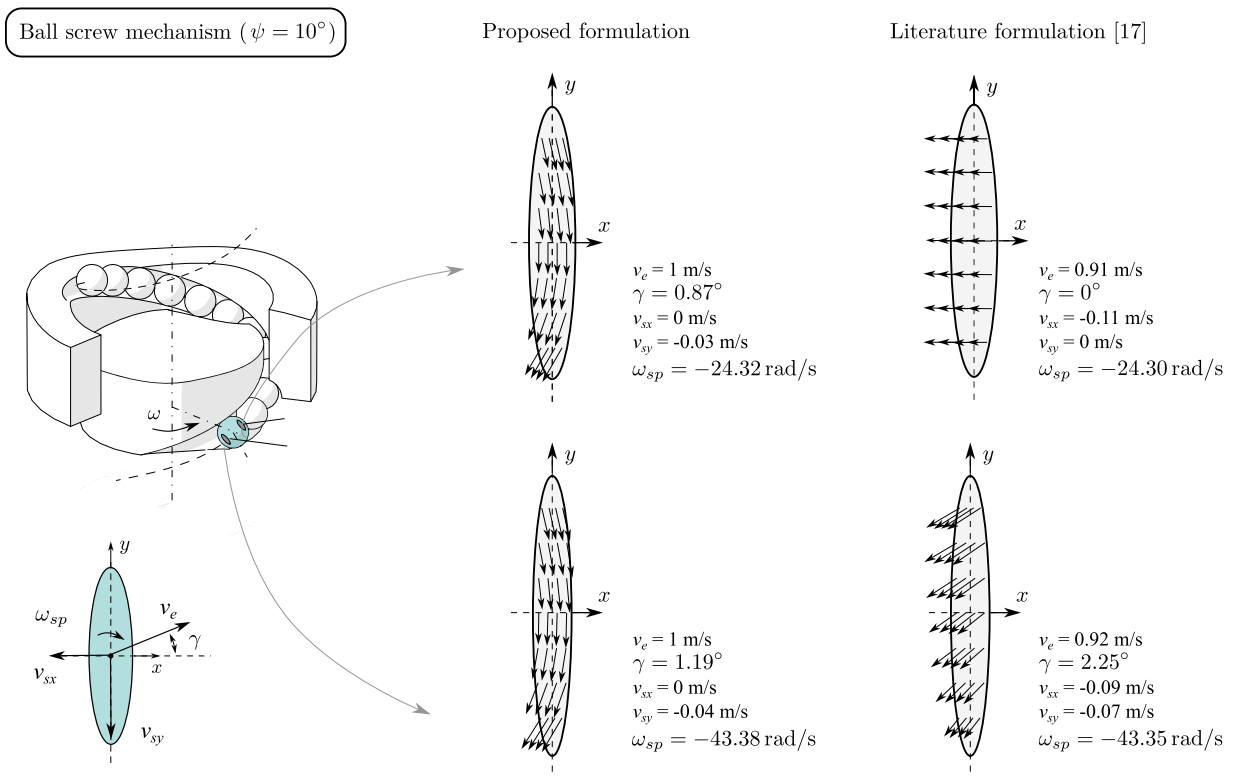

Fig. 8. Comparison of contact kinematics calculated using the literature and proposed formulations at ball screw scale (ψ = 10°).

To this end, the reference sliding speed distribution shown in Fig. 9-calculated at the inner contact in the previous section-is quantified using both the conventional *SRR* and the proposed three-parameter approaches. The limitations of each method are assessed by attempting to reconstruct the reference distribution based on the corresponding parameters.

For the reference case, the *SRR* calculated using the single-variable approach is 4.16 %. However, this parameter alone fails to capture the full complexity of the contact kinematics, leading to ambiguity in the reconstructed velocity field. As illustrated in Fig. 9, three distinct sliding speed distributions yield the same *SRR* value. This clearly demonstrates that the single *SRR* approach cannot account for the combined effects of rolling, spinning, and side slip. In particular, the spinning component is entirely neglected, resulting in different sliding patterns despite identical *SRR* magnitudes.

Moreover, the *SRR* approach lacks directional information. Multiple combinations of rolling and side slip can produce the same *SRR* value, further reinforcing its inherent ambiguity. Although only three examples are shown, infinitely many distributions could correspond to a given *SRR*, rendering it unsuitable for accurately characterising contact kinematics in ball screw mechanisms.

In contrast, the proposed three-parameter framework individually quantifies the rolling, side, and spinning slip components. These variables fully define the kinematic state at the contact, enabling a unique and unambiguous reconstruction of the sliding speed distribution.

The proposed parameters offer a robust and physically meaningful basis for linking contact kinematics conditions to key phenomena such as friction, wear, and lubrication. Their accurate determination is essential for realistic kinematic modelling and for improving the performance, durability, and reliability of ball screw mechanisms.

4.3. Influence of the kinematic constraints on contact kinematics

In this section, a parametric analysis is conducted to examine the influence of the kinematic constraints-r', β, and β'-on each sliding speed component. The study consists of three cases, each isolating the effect of one constraint while keeping the others fixed, thus allowing for an independent evaluation of their impact on contact kinematics.

4.3.1. Influence of the pure rolling radius (r'):

Fig. 10 shows the effect of the pure rolling radius (r') on the contact kinematics. In this analysis, r' is varied across a range of values, while the pitch angle (β) and yaw angle (β') are held constant. It should be noted that each contact-inner and outer-is

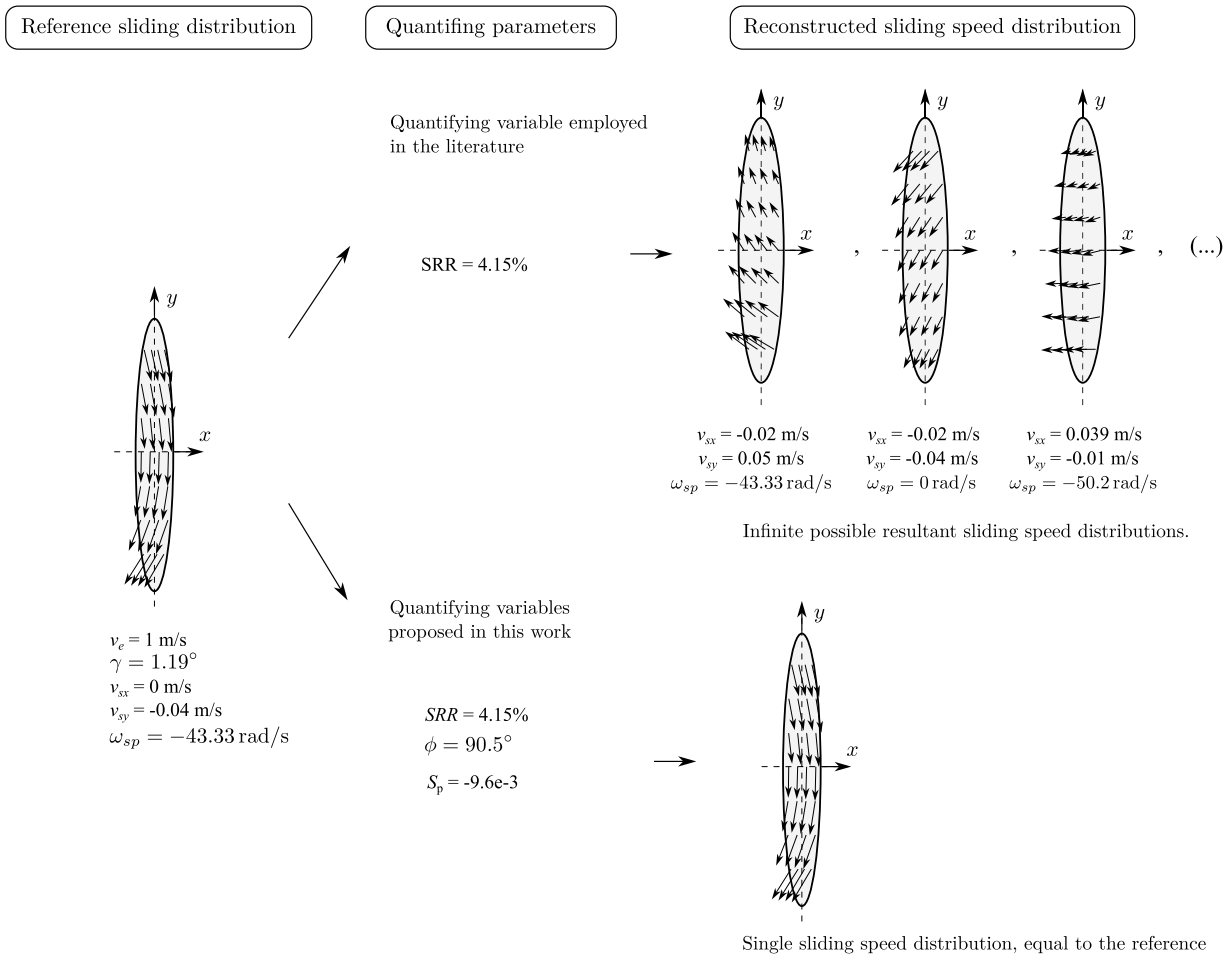

Fig. 9. Comparison of the employment of a single *SRR* and the three variable approach proposed in this work.

characterised by its own pure rolling radius, making this parameter independent for each interface. Therefore, although the results in Fig. 10 correspond to the inner contact, the same trends apply to the outer contact.

Fig. 10(a) presents the evolution of the quantifying parameters as a function of r'. Among these, the *SRR* direction (ϕ) is the most sensitive to variations in the r'. When $r' = D/2$-a value commonly adopted in the literature-ϕ approaches 90°, indicating that the *SRR* vector is aligned predominantly in the transverse direction. As r' decreases below $D/2$, ϕ shifts to values below 90°, corresponding to a vector with a positive x-component. Conversely, for values of r' above $D/2$, ϕ exceeds 90°, indicating a negative x-component. The *SRR* magnitude also exhibits slight sensitivity to r', while the remaining parameters-the entrainment speed, its orientation (γ), and the spin-to-roll ratio-remain essentially unaffected across the analysed range.

Fig. 10(b) illustrates three selected cases from the analysed r' range, focusing on the resulting sliding speed distributions and their breakdown into rolling, side, and spinning components. The total sliding speed field remains qualitatively similar across the three cases.

A more detailed interpretation is obtained by examining the individual sliding speed components. The results show that r' exclusively influences the rolling slip, while the side and spinning components remain unchanged. This parameter governs the position of the rolling velocity profile along the x-axis of the contact. As r' varies, the entire rolling profile shifts upward or downward without altering its shape. Notably, the value $r' \simeq D/2$ places the pure rolling points near the centre of the contact ellipse, consistent with common modelling assumptions in the literature.

4.3.2. *Influence of the yaw angle (β')*

Fig. 11 shows the effect of the yaw angle (β') on the contact kinematics. In this analysis, β' is varied while keeping the pure rolling radius (r') and pitch angle (β) constant.

Fig. 11(a) presents the evolution of the quantifying parameters as a function of the yaw angle (β'). It can be observed that β' has a marked influence on the direction of the entrainment speed (γ), as well as on both the magnitude and direction of the *SRR* (ϕ).

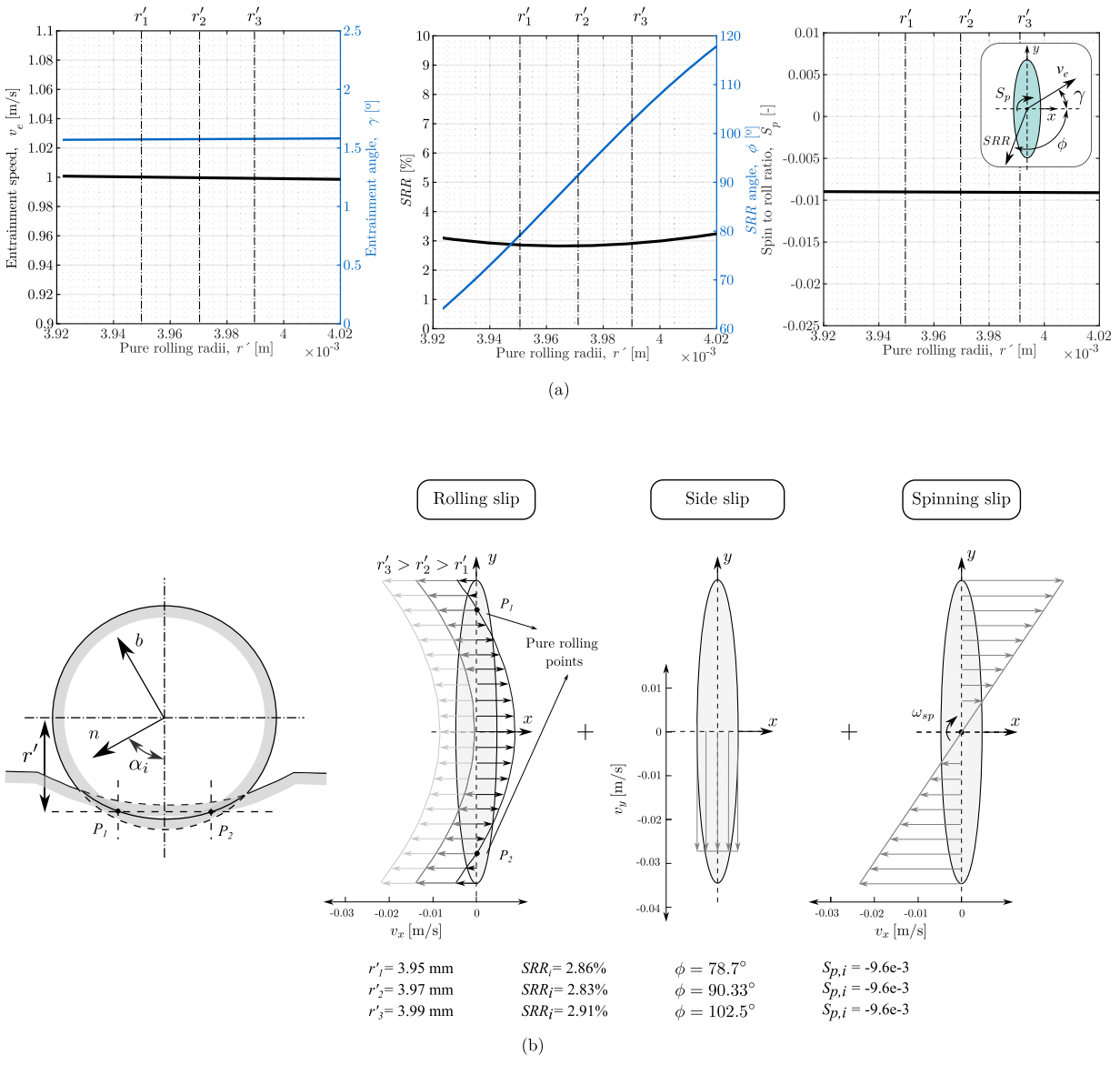

Fig. 10. Influence of the pure rolling radii (r') on: (a) *SRR* quantifying parameters and (b) on the composition of the sliding speed distribution.

Focusing on the entrainment vector, the angle γ remains within the range of 0° to 2.5°, exhibiting opposite trends at the inner and outer contacts as β' varies.

The most significant effect of β' appears in the *SRR*. Both its magnitude and direction show strong sensitivity to variations in yaw angle. At the outer contact, the *SRR* magnitude decreases from 0.8 % to nearly zero as β' increases from −3° to 3°. In contrast, the inner contact displays an increasing trend over the same range. A critical condition arises when $\beta' \approx -2.4°$, at which point the *SRR* at the outer contact becomes zero. In this case, the trend of the *SRR* angle ϕ becomes asymptotic, as the sliding vector vanishes and ϕ tends towards infinity.

Fig. 11(b) illustrates three selected cases from the analysed β' range, focusing on the resulting sliding speed distributions and their breakdown into rolling, side, and spinning components. The sliding behaviour differs significantly across the selected yaw angle values, demonstrating that β' has a considerable influence on contact kinematics.

Interpreting this sliding pattern requires a detailed examination of the individual sliding speed components. The results show that the yaw angle (β') uniquely governs the side slip component, while the rolling and spinning components remain unaffected. The effect of β' on side slip is opposite at the two contact interfaces. At the outer contact, an increase in β' leads to a rise in the transverse velocity component, thereby enhancing side slip. In contrast, the inner contact experiences a reduction in side slip with increasing yaw angle. As a result, there exists a specific value of β' for which side slip is entirely cancelled at one of the contacts. However, since

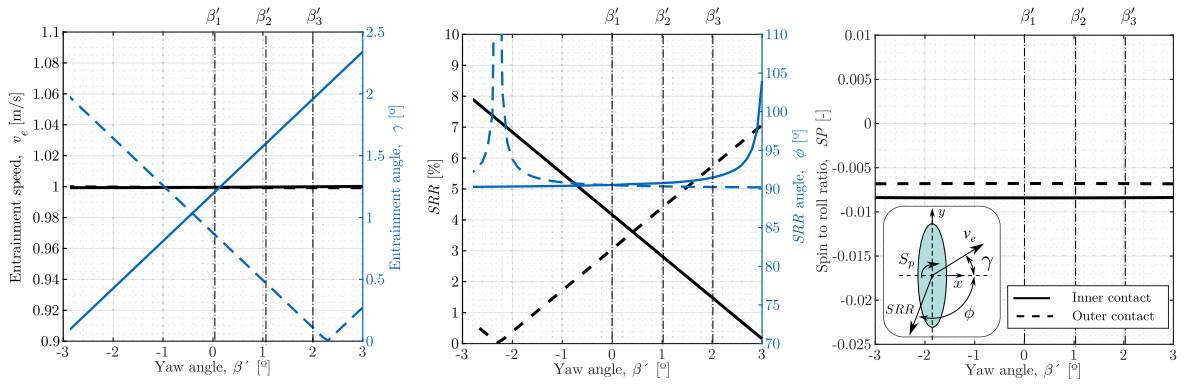

(a)

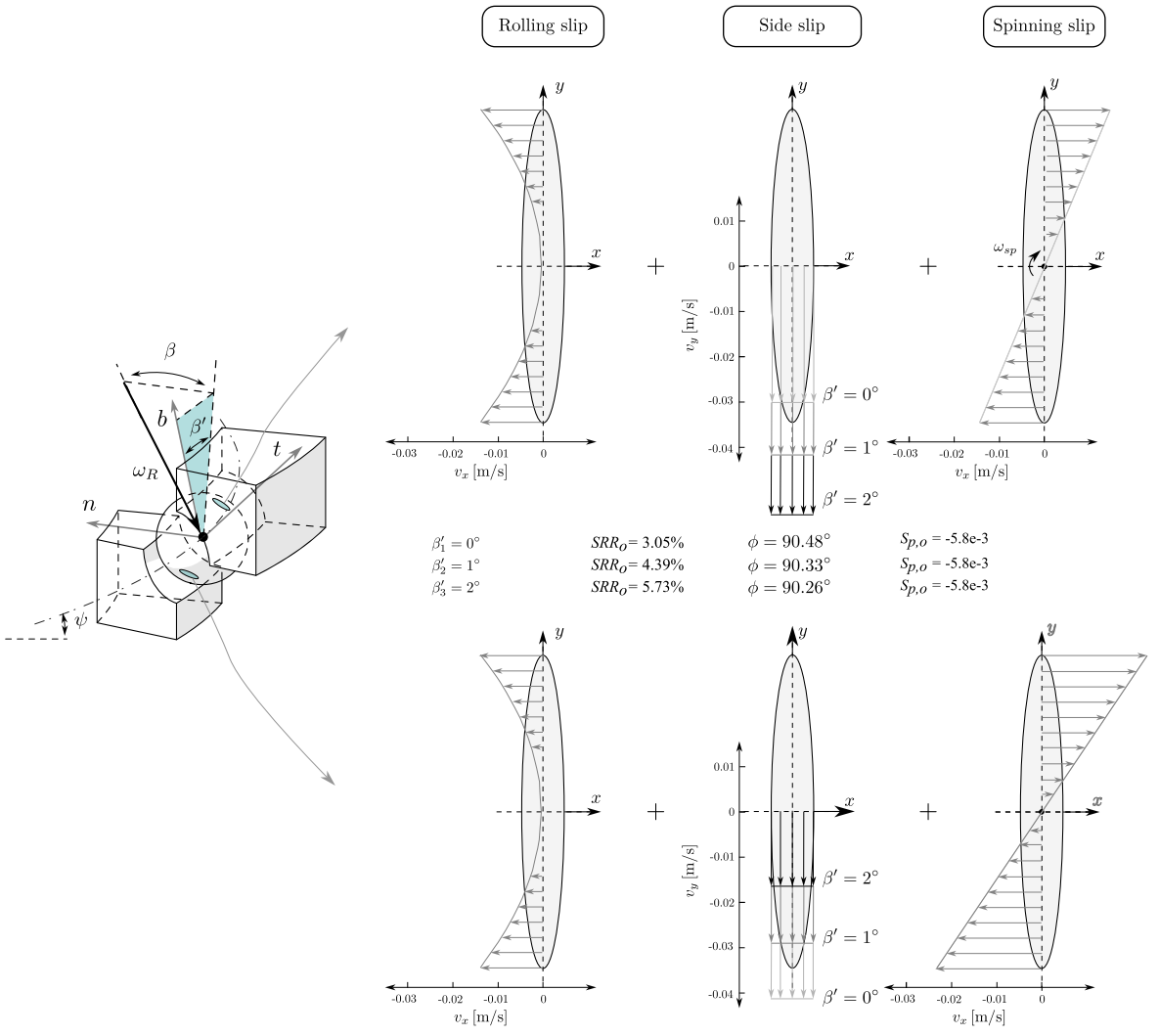

(b)

Fig. 11. Influence of the yaw angle (β') on: (a) *SRR* quantifying parameters and (b) on the composition of the sliding speed distribution.

the yaw angle is a global parameter, this cancellation cannot occur simultaneously at both interfaces. In the present case study, side slip vanishes at the outer contact for $\beta' \approx -2.3°$, and at the inner contact for $\beta' \approx 3.1°$.

These results show that even small variations in the yaw angle (β') produce significant changes in side slip. This highlights β' as a critical parameter in determining the contact kinematics of ball screws, particularly through its role in controlling the side sliding component.

4.3.3. Influence of the pitch angle (β)

Fig. 12 illustrates the influence of the pitch angle (β) on the contact kinematics. In this analysis, β is varied across three representative values, while the pure rolling radius (r') and yaw angle (β') are held constant to isolate the effect of the pitch angle.

Fig. 12(a) presents the evolution of the quantifying parameters with respect to β. The pitch angle primarily affects the spin-to-roll ratio, reflecting its strong influence on the spinning slip component. As β increases, the spinning speed and corresponding spin-to-roll ratio increase at the outer contact, while the opposite trend is observed at the inner contact. A slight variation is also observed in the *SRR* magnitude at both contacts, although this effect is considerably smaller compared to that observed in the spin-to-roll ratio.

Fig. 12(b) shows three selected cases from the analysed range of pitch angles, focusing on the resulting sliding speed distributions and their breakdown into rolling, side and spinning components. The sliding speed distribution varies significantly with pitch angle, highlighting the strong influence of β on the overall contact kinematic state.

The analysis of the individual sliding components reveals that β has a dominant effect on the spinning slip, a slight influence on the side slip, and no observable impact on the rolling slip. A closer examination of the spinning component reveals opposite behaviours at the two contact interfaces. At the outer contact, an increase in pitch angle leads to a rise in spinning speed and a corresponding reduction in spinning slip. Conversely, at the inner contact, spinning slip also decreases with increasing β. As a result, it is possible to cancel spinning slip at one interface by adjusting β, but this inevitably increases it at the other.

As described in the case definition, the specific values analysed in Fig. 12(b) correspond to different pitch angle calculation methodologies adopted in the literature. Spinning slip at the outer contact becomes zero when $\beta \approx 34.3°$, corresponding to the outer raceway control hypothesis. In this case, however, the inner contact exhibits relatively high spinning slip due to the opposing influence of pitch angle on spinning speed. In contrast, spinning slip at the inner contact vanishes when $\beta \approx 50.1°$, which corresponds to the inner raceway control assumption. Under this condition, spinning slip at the outer contact becomes substantial. For the other two pitch angle values analysed, spinning slip is present at both contacts. However, the magnitudes differ in each case, resulting in substantially different sliding speed distributions.

5. Discussion on the effect of operational conditions

As described in Section 2.8, the revised contact kinematic formulation is evaluated from a given load state and absolute motion of the ball. This state is completely defined by load-related variables (W_k, α_k) and kinematic-related variables (r'_k, β', and β). These quantities are influenced by the operating conditions to which the ball screw is subjected. However, their relative importance for contact kinematics differs considerably.

The load dependent variables (W_k and α_k) have a negligible effect on contact kinematics. They primarily affect the size of the contact ellipse, while their influence on the sliding speed distribution is minor. As reviewed in the introduction, methods for calculating load state and contact angles under varying operating conditions are already well established and validated in the literature [5,18,36,45].

In contrast, as demonstrated in Section 4.3, the kinematic constraints (r'_k, β', and β) have a governing effect on the sliding speed distribution. Therefore, the analysis of the effect of operational conditions is conducted highlighting these variables. An overview is given below to illustrate how operating conditions affect these kinematic constraints and the resultant sliding speed distribution of the contact. As described in Sec, several method exists in the literature to calculate these variables. Therefore, the analysis of operational conditions is conducted with all the existing models presented in Table 1. Each kinematic constraint is discussed independently:

- **Pure rolling radii (r'_k):** The literature assumes constant $r'_k = D/2$ for all geometry and operational conditions. Although this simplification is common, Section 4.3 shows that even small deviations of r', shift the rolling slip distribution and alter the position of the pure rolling points.
- **Yaw angle (β'):** Similarly, the literature assumes a yaw angle equal to zero for all operational conditions. However, Section 4.3 demonstrates that this variable has a decisive influence on the transverse slip component. Small variations can induce substantial changes in side slip, yet no methodology exists in the ball screw literature to relate β' to operating conditions.
- **Pitch angle (β):** As discussed in Section 2.8, several strategies are available in the literature to estimate the pitch angle under varying operating conditions. Fig. 13 illustrates the evolution of the pitch angle as a function of axial load for two rotational speeds, predicted by these methodologies. The results show that the trends obtained from each method differ considerably.

  To further highlight these discrepancies, the figure also presents the sliding speed distributions calculated with each method at 1500 N and 1000 rpm. All the analysed formulations predict different values for the pitch angle. The IRC and ORC approaches provide the upper and lower limiting predictions, respectively, and show very limited sensitivity to changes in operating conditions. The GEO and DAL approaches yield results closely aligned with those of the CONST formulation, and the operating conditions have only a minor effect on their pitch angle predictions. In contrast, the ITE method exhibits the highest sensitivity to operating conditions. When examining the sliding-speed distributions, substantial differences are observed in the predictions of each method under the same operating conditions.

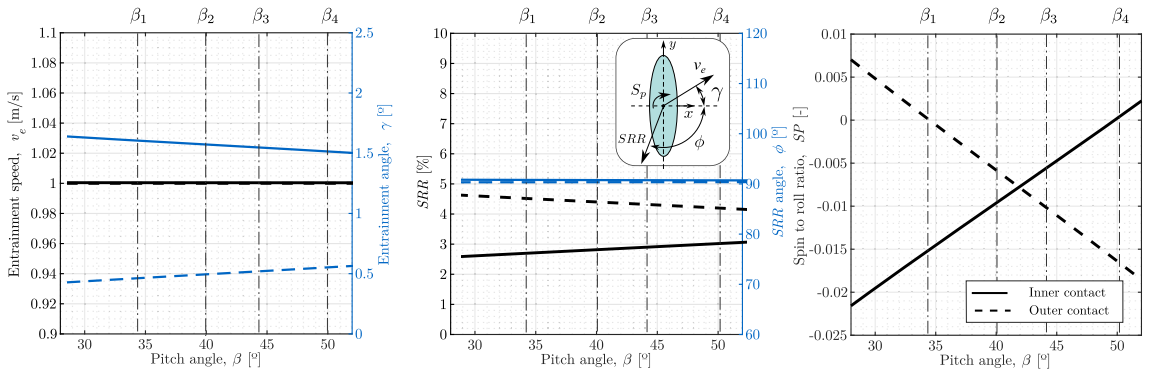

(a)

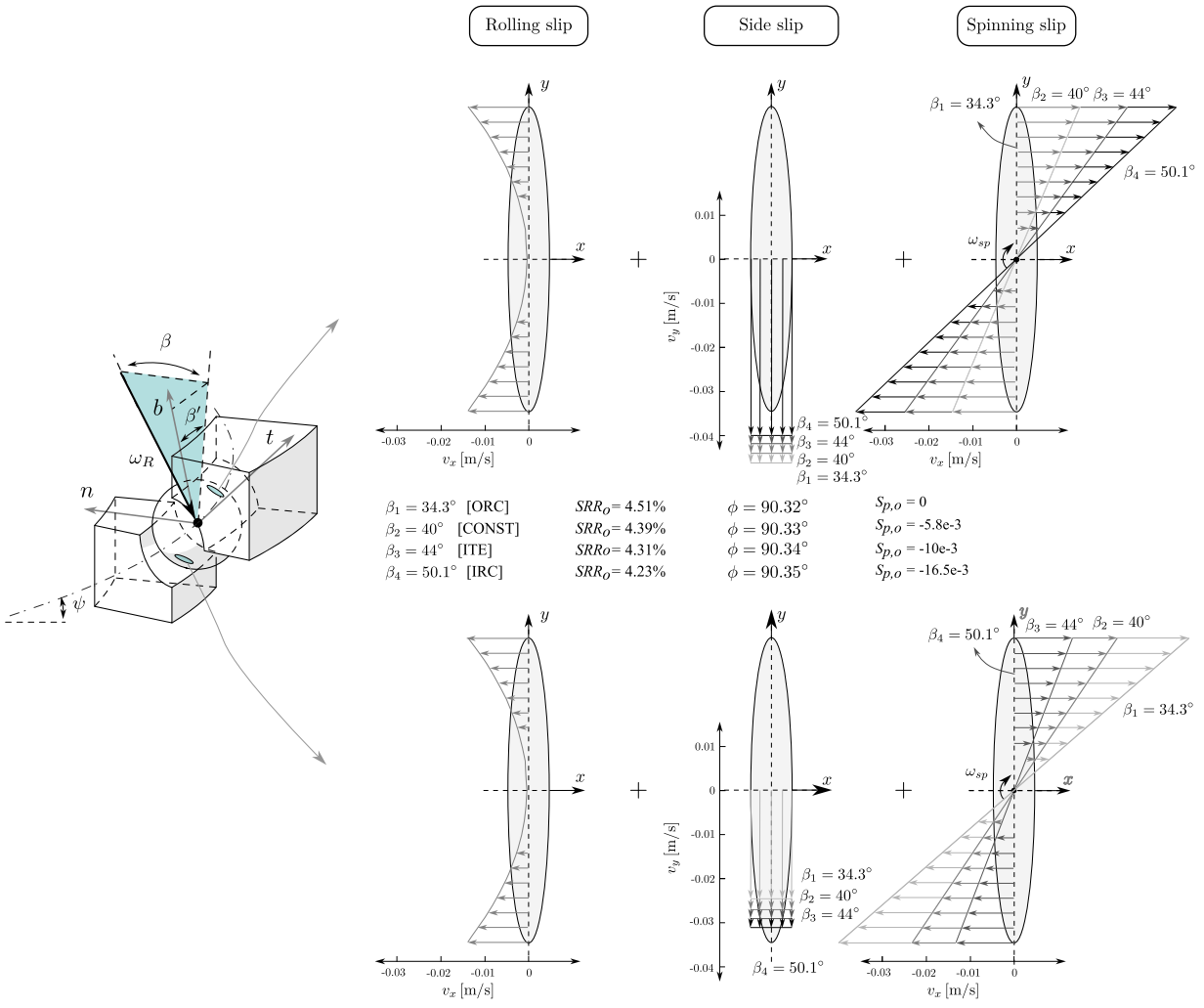

(b)

Fig. 12. Influence of the pitch angle (β') on: (a) *SRR* quantifying parameters and (b) on the composition of the sliding speed distribution.

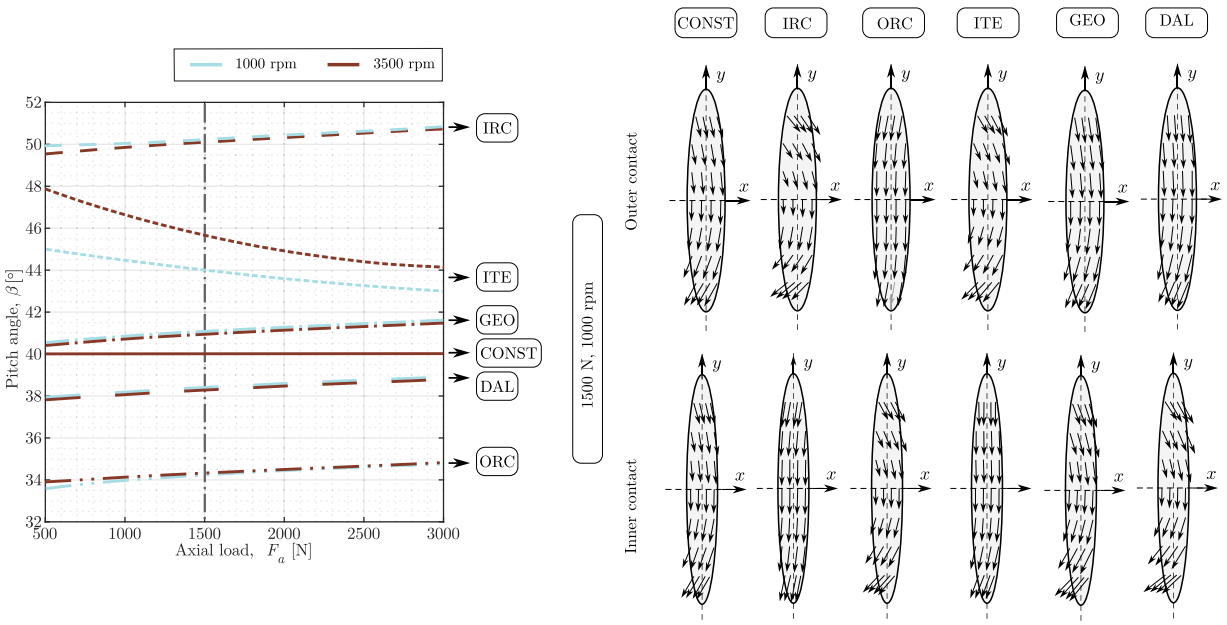

Fig. 13. Influence of axial load and angular velocity on the pitch angle and the resultant contact interface kinematics, for different assumptions available in the literature.

In the case of ball bearings, it has been reported that the IRC hypothesis provides accurate results at low speeds, whereas at high speeds the ORC hypothesis is more suitable [79,86]. However, to the authors' knowledge, no universally accepted criterion currently exists in the ball screw literature.

This comparison shows that kinematic constraints can be a source of uncertainty in predicting contact kinematics. Most models simplify the problem by assuming r'_k and β' as constant for all operational conditions, while offering alternative formulations only for β. However, the present study demonstrates that yaw angle and pure rolling radii are equally influential on contact kinematics. Despite their importance, however, no validated methodology currently exists to determine these parameters under realistic operating conditions. Furthermore, all existing approaches neglect frictional interactions, including lubricant viscosity, when calculating the kinematic constraints, which does not fully reflect the physical reality.

Future work should therefore focus on developing accurate procedures to evaluate r'_k, β', and β in practical operating regimes, including the effect of frictional interactions. Such advances are essential for improving predictive models of friction, wear, and lubrication, and ultimately for enhancing the performance and reliability of ball screw mechanisms.

In addition, experimental validation of contact kinematics remains a significant challenge in rolling-element mechanisms, such as ball bearings and ball screws, due to their confined and optically inaccessible nature. Future studies are therefore encouraged to advance experimental techniques in this field.

6. Conclusion

In this work, a revised formulation is presented to accurately compute the sliding speed distribution within the contact interface of ball screw mechanisms. The proposed model addresses previously identified inaccuracies and offers a comprehensive framework for calculating the sliding speed distribution across the entire contact interface. Moreover, the sliding speed distribution is broken down into its fundamental components-rolling, side, and spinning slip-to provide physical insight into the nature of contact kinematics. In addition, a new set of variables are introduced to quantify sliding behaviour at the contact, where three independent variables are proposed to characterise the contact kinematics. The following conclusions are drawn:

- The revised formulation is validated using an angular contact ball bearing configuration, which represents a special case of a ball screw with zero helix angle. While the traditional ball screw formulation fails to match the actual sliding speed distribution, the revised approach replicates the results observed in well-established ball bearing formulations, confirming the validity and consistency of the proposed formulation. When contact kinematics is analysed at ball screw level with the revised formulation, the conventional understanding of sliding speed distribution fundamentally changes. As demonstrated, both the magnitude and direction of the sliding velocity vectors are significantly altered, with side slip emerging as the dominant component.
- This study demonstrates that the conventional use of a single *SRR* is insufficient to accurately characterise the complex sliding behaviour present in ball screw mechanisms. A single *SRR* value cannot account for the combined and independent effects of rolling, side and spinning slip, leading to ambiguity in the representation of contact kinematics. The proposed three-parameter

framework addresses this limitation by separately quantifying each slip component, enabling a complete accurate reconstruction of the sliding speed distribution.

- The relationship between the key kinematic constraints-pure rolling radius, yaw angle, and pitch angle-and contact kinematics has been clearly established. Each variable predominantly influences a specific quantifying parameter: the pure rolling radius governs the *SRR*, the yaw angle modulates the *SRR* angle, and the pitch angle determines the Spin-to-Roll Ratio. Furthermore, the study demonstrates that each key kinematic constraints predominantly governs a specific component of the total sliding speed distribution. The pure rolling radius primarily governs rolling slip, the pitch angle influences the spinning speed, and the yaw angle controls the side slip.
- These findings underscore the sensitivity of contact kinematics to key kinematic constraints. In particular, the pronounced influence of yaw angle on side slip challenges the validity of common assumptions in the literature, such as a constant zero yaw angle and constant pure rolling radii for all the operational conditions. With respect to pitch angle, the literature-based comparison revealed substantial variations in the predicted sliding speed distributions depending on the estimation method. Despite the importance of the kinematic constraints, there is currently no validated methodology in the literature for accurately determining these variables under realistic operating and lubrication conditions.

Therefore, future research should focus on developing more accurate methodologies to determine these kinematic constraints. They should investigate the influence of lubricant rheology on contact kinematics to extend the predictive capabilities of the contact kinematic under realistic operating conditions. Such advances are essential for deepening the understanding of contact kinematics and for improving predictive models of friction, wear, and lubrication, ultimately enhancing the performance and reliability of ball screw systems. In addition, experimental validation of contact kinematics remains a significant challenge in rolling-element mechanisms, such as ball bearings and ball screws, due to their confined and optically inaccessible nature. Future studies are therefore encouraged to advance experimental techniques in this field.

CRediT authorship contribution statement

Pello Alberdi: Writing – review & editing, Writing – original draft, Visualization, Software, Methodology, Investigation, Formal analysis, Data curation, Conceptualization; **Aitor Arana:** Writing – review & editing, Supervision, Resources, Project administration, Methodology, Investigation, Funding acquisition, Formal analysis, Conceptualization; **Aitor Oyanguren:** Writing – review & editing, Resources, Project administration, Methodology, Investigation, Funding acquisition, Formal analysis, Conceptualization; **Jon Larrañaga:** Writing – review & editing, Resources, Project administration, Methodology, Investigation, Funding acquisition, Formal analysis, Conceptualization; **Ibai Ulacia:** Writing – review & editing, Supervision, Resources, Project administration, Methodology, Investigation, Funding acquisition, Formal analysis, Conceptualization.

Data availability

Data will be made available on request.

Declaration of competing interest

The authors declare that they have no known competing financial interests or personal relationships that could have appeared to influence the work reported in this paper.

Acknowledgments

The authors express their deep gratitude to Shuton, S.A and the Basque Government for partially funding the research under the projects SCALEROLL of the PUE program (ref. PUE_2020_1_0011), BISUM II of the Elkartek program (ref. KK-2024/00048) and PREVARHU of the Hazitek program (ref. ZL-2022/00996 and ZL-2023/00617).

References

[1] T.L. Nguyen, S.-K. Ro, J.-K. Park, Study of ball screw system preload monitoring during operation based on the motor current and screw-nut vibration, Mech. Syst. Signal Process. 131 (2019) 18–32. https://doi.org/10.1016/j.ymssp.2019.05.036.
[2] C. Li, M. Xu, W. Song, H. Zhang, A review of static and dynamic analysis of ball screw feed drives, recirculating linear guideway, and ball screw, Int. J. Mach. Tools Manuf. 188 (2023) 104021. https://doi.org/10.1016/j.ijmachtools.2023.104021.
[3] C.-G. Zhou, H.-T. Feng, Z.-T. Chen, Y. Ou, Correlation between preload and no-load drag torque of ball screws, Int. J. Mach. Tools Manuf. 102 (2016) 35–40. https://doi.org/10.1016/j.ijmachtools.2015.11.010.
[4] C.E. Okwudire, Y. Altintas, Hybrid modeling of ball screw drives with coupled axial, torsional, and lateral dynamics, J. Mech. Des. 131 (7) (2009) 071002. https://doi.org/10.1115/1.3125887.
[5] A.C. Bertolino, G. Jacazio, S. Mauro, M. Sorli, Investigation on the ball screws no-load drag torque in presence of lubrication through MBD simulations, Mech. Mach. Theory 161 (2021) 104328. https://doi.org/10.1016/j.mechmachtheory.2021.104328.
[6] J. Zhao, M. Lin, X. Song, Q. Guo, Investigation of load distribution and deformations for ball screws with the effects of turning torque and geometric errors, Mech. Mach. Theory 141 (2019) 95–116. https://doi.org/10.1016/j.mechmachtheory.2019.07.006.
[7] A.C. Bertolino, M. Sorli, G. Jacazio, S. Mauro, Lumped parameters modelling of the EMAs' ball screw drive with special consideration to ball/grooves interactions to support model-based health monitoring, Mech. Mach. Theory 137 (2019) 188–210. https://doi.org/10.1016/j.mechmachtheory.2019.03.022.

[8] M. Azamfar, X. Li, J. Lee, Intelligent ball screw fault diagnosis using a deep domain adaptation methodology, Mech. Mach. Theory 151 (2020) 103932. https://doi.org/10.1016/j.mechmachtheory.2020.103932.
[9] P. Li, X. Jia, J. Feng, H. Davari, G. Qiao, Y. Hwang, J. Lee, Prognosability study of ball screw degradation using systematic methodology, Mech. Syst. Signal Process. 109 (2018) 45–57. https://doi.org/10.1016/j.ymssp.2018.02.046.
[10] W. Zhang, M. Xu, H. Yang, X. Wang, S. Zheng, X. Li, Data-driven deep learning approach for thrust prediction of solid rocket motors, Measurement 225 (2024) 114051. https://doi.org/10.1016/j.measurement.2023.114051.
[11] C. Liu, X. Li, X. Chen, S. Khan, Neuromorphic computing-enabled generalized machine fault diagnosis with dynamic vision, Adv. Eng. Inf. 65 (2025) 103300. https://doi.org/10.1016/j.aei.2025.103300.
[12] W. Zhang, N. Jiang, S. Yang, X. Li, Federated transfer learning for remaining useful life prediction in prognostics with data privacy, Meas. Sci. Technol. (2025). https://doi.org/DOI10.1088/1361-6501/ade552.
[13] C.-C. Wei, W.-L. Liou, R.-S. Lai, Wear analysis of the offset type preloaded ball–screw operating at high speed, Wear 292 (2012) 111–123. https://doi.org/10.1016/j.wear.2012.05.024.
[14] L. Cao, K.-J. Oh, S.-C. Chung, Explicit precision friction torque model of ball screws in high speed operations, Tribol. Int. 152 (2020) 106573. https://doi.org/10.1016/j.triboint.2020.106573.
[15] G.A. Levit, Calculations of recirculating ball screw and nut transmissions, Mach. Tooling 34 (5) (1963) 9–16.
[16] Y.N. Drozdov, Calculating the wear of a screw and nut transmission with sliding friction, Soviet Eng. Res. 4 (5) (1984) 6–8.
[17] M.C. Lin, B. Ravani, S.A. Velinsky, Kinematics of the ball screw mechanism, J. Mech. Des. 116 (3) (1994) 849–855. https://doi.org/10.1115/1.2919459.
[18] C.C. Wei, J.F. Lin, Kinematic analysis of the ball screw mechanism considering variable contact angles and elastic deformations, J. Mech. Des. 125 (4) (2003) 717–733. https://doi.org/10.1115/1.1623761.
[19] S. Bair, C. McCabe, P.T. Cummings, Calculation of viscous EHL traction for squalane using molecular simulation and rheometry, Tribol. Lett. 13 (2002) 251–254. https://doi.org/10.1023/A:1021011225316.
[20] M. Björling, Friction in Elastohydrodynamic Lubrication, Ph.D. thesis, Luleå Tekniska Universitet, 2014.
[21] B. Wainwright, A. Kadiric, Surface fatigue in lubricated contacts: mapping the failure modes of micropitting versus macropitting, Int. J. Fatigue 197 (2025) 108908.
[22] S.G. Mu, X.Y. Feng, Analysis of elastohydrodynamic lubrication of ball screw with rotating nut, Appl. Mech. Mater. 121 (2012) 3132–3139. https://doi.org/10.4028/www.scientific.net/AMM.121-126.3132.
[23] J. Hu, M. Wang, T. Zan, The kinematics of ball-screw mechanisms via the slide–roll ratio, Mech. Mach. Theory 79 (2014) 158–172. https://doi.org/10.1016/j.mechmachtheory.2014.04.017.
[24] K. Deshun, W. Min, G. Xiangsheng, Effect of contact angle and helix angle on slide-roll ratio under the uniform motion state of BSM, in: MATEC Web of Conferences, 108, EDP Sciences, 2017, p. 04008.
[25] Q. Cheng, B. Qi, Z. Liu, C. Zhang, D. Xue, An accuracy degradation analysis of ball screw mechanism considering time-varying motion and loading working conditions, Mech. Mach. Theory 134 (2019) 1–23. https://doi.org/10.1016/j.mechmachtheory.2018.12.024.
[26] H. Wang, F. Li, Y. Cai, Y. Liu, Y. Yang, Experimental and theoretical analysis of ball screw under thermal effect, Tribol. Int. 152 (2020) 106503. https://doi.org/10.1016/j.triboint.2020.106503.
[27] J.-J. Zhao, M.-X. Lin, X.-C. Song, N. Wei, Coupling analysis of the fatigue life and the TEHL contact behavior of ball screw under the multidirectional load, Ind. Lubr. Tribol. 72 (10) (2020) 1285–1293. https://doi.org/10.1108/ILT-03-2020-0097.
[28] B.-B. Qi, Q. Cheng, S.-L. Li, Z.-F. Liu, C.-B. Yang, Precision loss of ball screw mechanism under sliding-rolling mixed motion behavior, J. Central South Univ. 28 (5) (2021) 1357–1376. https://doi.org/10.1007/s11771-020-4537-1.
[29] W. Wang, S. Chen, C. Lu, L. Lv, Discussion on ball screw slide–roll ratio and entrainment velocity calculation, Machines 10 (3) (2022) 203. https://doi.org/10.3390/machines10030203.
[30] J. Zhao, B. Qi, X. Song, H. Jiang, P. Dong, A modeling method for predicting friction torque of the preload double-nut ball screw based on thermal elastohydrodynamic lubrication, Int. J. Adv. Manuf. Technol. 124 (11) (2023) 4231–4251. https://doi.org/10.1007/s00170-022-09524-2.
[31] T. Harris, M. Kotzalas, Advanced Concepts of Bearing Technology. Rolling Bearing Analysis, CRC Press, 2006.
[32] M. Guessasma, C. Machado, Three-dimensional DEM modelling of ball bearing with lubrication regime prediction, Lubricants 6 (2) (2018) 46. https://doi.org/10.3390/lubricants6020046.
[33] T. Yoshida, Y. Tozaki, S. Matsumoto, Study on load distribution and ball motion of ball screw, Jpn. J. Tribol. 48 (4) (2003) 383–396.
[34] Y. Chen, W. Tang, Dynamic contact stiffness analysis of a double-nut ball screw based on a quasi-static method, Mech. Mach. Theory 73 (2014) 76–90. https://doi.org/10.1016/j.mechmachtheory.2013.10.008.
[35] A.C. Bertolino, S. Mauro, G. Jacazio, M. Sorli, Multibody dynamic model of a double nut preloaded ball screw mechanism with lubrication, in: ASME International Mechanical Engineering Congress and Exposition, 84553, American Society of Mechanical Engineers, 2020, p. V07BT07A023. https://doi.org/10.1115/IMECE2020-23619.
[36] J. Liu, Y. Ou, Dynamic axial contact stiffness analysis of position preloaded ball screw mechanism, Adv. Mech. Eng. 11 (1) (2019) 1687814018819289. https://doi.org/10.1177/1687814018819289.
[37] X. Mei, M. Tsutsumi, T. Tao, N. Sun, Study on the load distribution of ball screws with errors, Mech. Mach. Theory 38 (11) (2003) 1257–1269. https://doi.org/10.1016/S0094-114X(03)00070-3.
[38] C. Liu, C. Zhao, X. Meng, B. Wen, Static load distribution analysis of ball screws with nut position variation, Mech. Mach. Theory 151 (2020) 103893. https://doi.org/10.1016/j.mechmachtheory.2020.103893.
[39] B. Lin, C.E. Okwudire, J.S. Wou, Low order static load distribution model for ball screw mechanisms including effects of lateral deformation and geometric errors, J. Mech. Des. 140 (2) (2018) 022301. https://doi.org/10.1115/1.4038071.
[40] L. Sangalli, A. Oyanguren, J. Larranaga, A. Arana, M. Izquierdo, I. Ulacia, Numerical characterization of local and global non-uniformities in the load distribution in ball screws, Int. J. Adv. Manuf. Technol. 118 (5) (2022) 1411–1425. https://doi.org/10.1007/s00170-021-07978-4.
[41] L. Lv, S. Chen, C. Lu, W. Wang, Analysis of load distribution for ball screws with circulation modes and geometric errors, Mech. Mach. Theory 199 (2024) 105677. https://doi.org/10.1016/j.mechmachtheory.2024.105677.
[42] L. Sangalli, A. Oyanguren, M. Izquierdo, J. Larrañaga, I. Ulacia, Numerical study on the effectiveness of the optimization of the load distribution in ball screw actuators, Mech. Mach. Theory 203 (2024) 105781. https://doi.org/10.1016/j.mechmachtheory.2024.105781.
[43] C.C. Wei, J.F. Lin, J.-H. Horng, Analysis of a ball screw with a preload and lubrication, Tribol. Int. 42 (11-12) (2009) 1816–1831. https://doi.org/10.1016/j.triboint.2008.12.013.
[44] C.C. Wei, J.H. Horng, J.F. Lin, Kinematic and friction analyses of a ball screw with a preload and the EHL lubrication model, in: 17th International Colloquium Tribology 2010-Solving Friction and Wear Problems, 2010, pp. 78–84.
[45] C.C. Wei, R.-S. Lai, Kinematical analyses and transmission efficiency of a preloaded ball screw operating at high rotational speeds, Mech. Mach. Theory 46 (7) (2011) 880–898. https://doi.org/10.1016/j.mechmachtheory.2011.02.009.
[46] N. Xu, W. Tang, Y. Chen, D. Bao, Y. Guo, Modeling analysis and experimental study for the friction of a ball screw, Mech. Mach. Theory 87 (2015) 57–69. https://doi.org/10.1016/j.mechmachtheory.2014.12.019.
[47] N. Xu, W.C. Tang, Modeling and analyzing the slipping of the ball screw, Latin Am. J. Solids Struct. 12 (2015) 612–623. https://doi.org/10.1590/1679-78251292.
[48] L.-C. Zhang, C.-G. Zhou, Experimental study on the coefficient of friction of the ball screw, J. Tribol. 144 (3) (2022) 031601. https://doi.org/10.1115/1.4051157.
[49] D. Kong, M. Wang, X. Gao, Theoretical and experimental analysis of drag torque for accelerated motion of ball screw mechanism, Adv. Mech. Eng. 9 (12) (2017) 1687814017743112. https://doi.org/10.1177/1687814017743112.
[50] Y. Zhang, P. Cui, J. Yang, Z. Wang, W. Pu, Dynamic grease lubrication and friction behavior of ball screw mechanism in high-frequency reciprocating motion, Tribol. Int. 178 (2023) 108068. https://doi.org/10.1016/j.triboint.2022.108068.

[51] J. Zhao, M. Lin, X. Song, Q. Guo, Analysis of the precision sustainability of the preload double-nut ball screw with consideration of the raceway wear, Proc. Inst. Mech. Eng. Part J: J. Eng. Tribol. 234 (9) (2020) 1530–1546. https://doi.org/10.1177/1350650119883484.
[52] C.-G. Zhou, H.-X. Zhou, H.-T. Feng, Experimental analysis of the wear coefficient of double-nut ball screws, Wear 446 (2020) 203201. https://doi.org/10.1016/j.wear.2020.203201.
[53] H.-X. Zhou, C.-G. Zhou, H.-T. Feng, Y. Ou, Theoretical and experimental analysis of the preload degradation of double-nut ball screws, Precis. Eng. 65 (2020) 72–90. https://doi.org/10.1016/j.precisioneng.2020.04.012.
[54] Y. Liu, C. Yang, T. Zhang, Q. Cheng, Z. Liu, Y. Zhao, Analysis of precision loss of double-nut ball screw considering dimensional error and preload degradation, J. Tribol. 147 (12) (2025). https://doi.org/10.1115/1.4066303.
[55] P. Alberdi, A. Arana, A. Oyanguren, J. Larrañaga, I. Ulacia, Redefining ball screw kinematics: analysing the limitations of traditional formulations for orbital and angular speed, Mech. Mach. Theory 205 (2025) 105882. https://doi.org/10.1016/j.mechmachtheory.2024.105882.
[56] M. Kolivand, A. Kahraman, A load distribution model for hypoid gears using ease-off topography and shell theory, Mech. Mach. Theory 44 (10) (2009) 1848–1865. https://doi.org/10.1016/j.mechmachtheory.2009.03.009.
[57] M. Mohammadpour, S. Theodossiades, H. Rahnejat, Elastohydrodynamic lubrication of hypoid gear pairs at high loads, Proc. Inst. Mech. Eng. Part J: J. Eng. Tribol. 226 (3) (2012) 183–198. https://doi.org/10.1177/1350650111431027.
[58] M. Raghavan, Kinematics of the full-toroidal traction drive variator, in: International Design Engineering Technical Conferences and Computers and Information in Engineering Conference, 35203, American Society of Mechanical Engineers, 2000, pp. 1073–1080. https://doi.org/10.1115/DETC2000/MECH-14170.
[59] G. Carbone, L. Mangialardi, G. Mantriota, A comparison of the performances of full and half toroidal traction drives, Mech. Mach. Theory 39 (9) (2004) 921–942. https://doi.org/10.1016/j.mechmachtheory.2004.04.003.
[60] L. De Novellis, G. Carbone, L. Mangialardi, Traction and efficiency performance of the double roller full-toroidal variator: a comparison with half-and full-toroidal drives, J. Mech. Des. (2012). https://doi.org/10.1115/1.4006791.
[61] M. Omasta, I. Křupka, M. Hartl, Effect of surface velocity directions on elastohydrodynamic film shape, Tribol. Trans. 56 (2) (2013) 301–309. https://doi.org/10.1080/10402004.2012.750024.
[62] M. Omasta, I. Křupka, M. Hartl, Effect of sliding direction on EHL film shape under high sliding conditions, Tribol. Trans. 60 (1) (2017) 87–94. https://doi.org/10.1080/10402004.2016.1147110.
[63] A. Porras-Vazquez, D. Philippon, N. Fillot, P. Vergne, N. Devaux, L. Lafarge, G.E. Morales-Espejel, An experimental approach to evaluate film thickness in starved large-size spinning contacts, J. Tribol. 144 (11) (2022) 111604. https://doi.org/10.1115/1.4054863.
[64] M. Iribecampos, I. Ulacia, A. Arana, The combined effect of contact interface size and spin on lubricated traction in rolling-sliding point contacts Tribol. Int.188 (2023) 108822. https://doi.org/10.1016/j.triboint.2023.108822.
[65] S.H. Loewenthal, Spin analysis of concentrated traction contacts J. Mech., Trans., and Automation.108 (1986) 77-84. https://doi.org/10.1115/1.3260788.
[66] R.I. Popovici, Friction in Wheel - Rail Contacts, Phd thesis - research ut, graduation ut, University of Twente, 2010. https://doi.org/10.3990/1.9789036529570.
[67] M. Omasta, I. Krupka, M. Hartl, Study of elastohydrodynamic film shape under different directions of velocity vectors, in: International Joint Tribology Conference, 54747, 2011, pp. 401–403. https://doi.org/10.1115/IJTC2011-61259.
[68] A. Porras-Vazquez, N. Fillot, P. Vergne, D. Philippon, G.E. Morales-Espejel, Influence of spin on film thickness in elastohydrodynamic starved point contacts, Tribol. Int. 156 (2021) 106825. https://doi.org/10.1016/j.triboint.2020.106825.
[69] Y. Higashitani, S. Kawabata, M. Björling, A. Almqvist, Effect of entrainment sliding direction to the traction coefficient for elastohydrodynamic lubrication elliptical contacts in the linear isothermal region, J. Tribol. 146 (12) (2024). https://doi.org/10.1115/1.4065661.
[70] K.L. Johnson, Contact Mechanics, Cambridge university press, 1985. https://doi.org/10.1017/CBO9781139171731.
[71] A.C. Bertolino, A. De Martin, S. Mauro, M. Sorli, Derivation of the exact curvature formulation for gothic arch ball screw grooves, in: ASME International Mechanical Engineering Congress and Exposition, 86649, American Society of Mechanical Engineers, 2022, p. V02BT02A044. https://doi.org/10.1115/IMECE2022-95746.
[72] A.C. Bertolino, A. De Martin, S. Mauro, M. Sorli, Exact formulation for the curvature of gothic arch ball screw profiles and new approximated solution based on simplified groove geometry, Machines 11 (2) (2023) 261. https://doi.org/10.3390/machines11020261.
[73] M.C. Lin, B. Ravani, S.A. Velinsky, Design of the ball screw mechanism for optimal efficiency, J. Mech. Des. 116 (3) (1994) 856–861. https://doi.org/10.1115/1.2919460.
[74] J. Liu, X. Li, S. Ding, R. Pang, A time-varying friction moment calculation method of an angular contact ball bearing with the waviness error, Mech. Mach. Theory 148 (2020) 103799. https://doi.org/10.1016/j.mechmachtheory.2020.103799.
[75] W.Z. Wang, L. Hu, S.G. Zhang, L.J. Kong, Modeling high-speed angular contact ball bearing under the combined radial, axial and moment loads, Proc. Inst. Mech. Eng. Part C: J. Mech. Eng. Sci. 228 (2014). https://doi.org/10.1177/0954406213490874.
[76] P. Alberdi, A. Arana, A. Oyanguren, J. Larrañaga, I. Ulacia, A general kinematic model for lubricated ball bearings based on the minimum energy hypothesis, Tribol. Int. 196 (2024) 109698. https://doi.org/10.1016/j.triboint.2024.109698.
[77] J. Liu, C. Tang, H. Wu, Z. Xu, L. Wang, An analytical calculation method of the load distribution and stiffness of an angular contact ball bearing, Mech. Mach. Theory 142 (2019) 103597. https://doi.org/10.1016/j.mechmachtheory.2019.103597.
[78] C.A. Foord, High-speed ball bearing analysis, Proc. Inst. Mech. Eng. Part G: J. Aerosp. Eng. 220 (2006) 537–544. https://doi.org/10.1243/09544100G01805.
[79] W. Wang, L. Hu, S. Zhang, Z. Zhao, S. Ai, Modeling angular contact ball bearing without raceway control hypothesis, Mech. Mach. Theory 82 (2014) 154–172. https://doi.org/10.1016/j.mechmachtheory.2014.08.006.
[80] Shuton, XP catalogue, 2024, (Catalogue).
[81] NSK Corporation, Ball screw catalogue, 2021, (Catalogue).
[82] Thompson, Precision ball screws and lead screws, 2024, (Catalogue).
[83] Umbra Group, Industrial ball screws catalogue, 2021, (Catalogue).
[84] Steinmeyer, Steinmeyer ball Screws, 2017, (Catalogue).
[85] F. Meng, Y. Zheng, Y. Liu, J. Gong, B. Wang, Multi-ellipsoid contact elastohydrodynamic lubrication performance for deep groove ball bearing, Tribol. Int. 150 (2020) 106367. https://doi.org/10.1016/j.triboint.2020.106367.
[86] A. Popescu, L. Houpert, D. Olaru, Four approaches for calculating power losses in an angular contact ball bearing, Mech. Mach. Theory 144 (2020) 103669. https://doi.org/10.1016/j.mechmachtheory.2019.103669.